JAMES | Journal of Advances in Modeling Earth Systems®

RESEARCH ARTICLE
10.1029/2025MS005515

Key Points:

- An analytical model is developed, which concisely represents the impact of small-scale bathymetry on large-scale circulation patterns
- The theory-based parameterization is implemented in the HYbrid Coordinate Ocean Model
- The proposed closure is tested on the canonical vortex spin-down problem

Correspondence to:
T. Radko,
tradko@nps.edu

Citation:
Radko, T., Brown, J., Xu, X., & Chassignet, E. P. (2026). The sandpaper theory of flow-topography interaction: The non-local formulation. *Journal of Advances in Modeling Earth Systems*, *18*, e2025MS005515. https://doi.org/10.1029/2025MS005515

Received 19 SEP 2025
Accepted 23 MAR 2026

Author Contributions:
Conceptualization: Timour Radko, Eric P. Chassignet
Data curation: Justin Brown, Xiaobiao Xu
Formal analysis: Timour Radko
Funding acquisition: Timour Radko, Eric P. Chassignet
Investigation: Timour Radko, Justin Brown, Xiaobiao Xu
Methodology: Timour Radko
Project administration: Timour Radko, Eric P. Chassignet
Resources: Xiaobiao Xu, Eric P. Chassignet
Software: Justin Brown, Xiaobiao Xu
Supervision: Timour Radko, Eric P. Chassignet
Validation: Timour Radko, Justin Brown, Xiaobiao Xu
Visualization: Timour Radko, Xiaobiao Xu
Writing – original draft: Timour Radko

The Sandpaper Theory of Flow-Topography Interaction: The Non-Local Formulation

Timour Radko[1], Justin Brown[1], Xiaobiao Xu[2], and Eric P. Chassignet[2]

[1]Department of Oceanography, Naval Postgraduate School, Monterey, CA, USA, [2]Center for Ocean-Atmospheric Prediction Studies, Florida State University, Tallahassee, FL, USA

Abstract

The irregular seafloor variability at lateral scales of several kilometers can strongly influence large-scale oceanic flows. However, these fine topographic patterns are currently unresolved by most global circulation models. To address this complication, we develop the "sandpaper" model of flow-topography interaction. This theory uses asymptotic multiscale methods to parameterize the effects of small-scale bathymetry in analytical and coarse-resolution numerical models. The previously reported version of the sandpaper theory assumed that the direct effects of bottom roughness are limited to the deepest density layer. Its reliance on the local approximation fundamentally limited the model's ability to represent the vertical structure of abyssal flows. To overcome this deficiency, we develop a more general non-local model, in which the effects of bottom roughness are distributed throughout the water column. The non-local formulation enables the implementation of the sandpaper closure in isopycnal models designed for realistic simulations, in which density interfaces frequently intersect the bathymetry. Local closure in such regions exhibits unphysical singularities, whereas its non-local counterpart remains well-behaved. The non-local sandpaper model is implemented in the HYbrid Coordinate Ocean Model (HYCOM), one of the mainstream oceanographic general circulation models. The parameterization is tested on the canonical vortex spin-down problem.

Plain Language Summary

The ocean floor is not smooth. It is covered with ridges, seamounts, valleys, and other irregular features with horizontal scales of just a few kilometers. These small-scale patterns can significantly influence the movement of major ocean currents. Unfortunately, most numerical ocean models are too coarse to capture such fine bathymetric details directly. In this work, we develop the "sandpaper" theory that enables us to represent the effects of seafloor roughness without explicitly resolving it. Earlier versions of this model accounted for roughness effects only near the ocean bottom. However, this study extends the sandpaper theory to allow assessment of the direct impact of small-scale topography throughout the water column. We implement this improved non-local model in HYCOM, a widely used ocean general circulation model, and test it in an idealized setting. The new formulation yields more accurate results than the original model, offering an opportunity to enhance the representation of deep-ocean processes in global simulations.

1. Introduction

The impact of irregular small-scale ocean topography on large-scale circulation patterns can be surprisingly profound. Particularly striking are the cumulative effects of bathymetric patterns with a lateral scale of several kilometers, commonly referred to as seafloor roughness. Typical heights of these fine-scale bathymetric features range from tens to a few hundred meters (e.g., Goff, 2020)—on the order of 1–10% of the total ocean depth. Yet, they tangibly affect currents commensurate in strength to the Gulf Stream (LaCasce et al., 2019) and the Antarctic Circumpolar Current (Naveira Garabato et al., 2013). Several studies have emphasized the adverse impact of seafloor roughness on baroclinic instability of surface-intensified flows (Palóczy & LaCasce, 2022; Radko, 2024b). As a result, rough topography can modulate the intensity and spatial distribution of transient mesoscale variability, which dominates the kinetic energy budget of the World Ocean (e.g., Stammer, 1997; Storer et al., 2022). Seafloor roughness has also been invoked as a key factor in extending the lifespan of ocean rings and their ability to transport heat, nutrients, and pollutants across ocean basins (Gulliver & Radko, 2022). Roughness-induced drag also affects the structure and speed of planetary waves (Davis et al., 2025), underscoring the ubiquity of oceanic processes modulated by small-scale topography.

Despite a persistent stream of evidence implicating small-scale topography in various oceanic phenomena and a rising interest in the subject (He & Wang, 2024; LaCasce et al., 2024; Siegelman & Young, 2023; Zhang &

Writing – review & editing: Timour Radko, Justin Brown, Xiaobiao Xu, Eric P. Chassignet

Xie, 2024), our understanding of the fundamental physics remains limited. For instance, even traditional assumptions, such as a monotonic increase in bottom drag with flow speed, have been challenged. An argument has been made that, in certain regimes, roughness-induced drag is inversely proportional to abyssal velocity. This tendency could substantially affect the stability of large-scale flows and the resulting patterns throughout the entire water column (Radko, 2024a). Limited insight into dynamics can also compromise the more pragmatic objectives of flow-topography interaction studies. Of particular concern is the representation of the effects of rough topography in numerical Earth System Models (e.g., Mashayek, 2023). Despite continuous advancements in high-performance computing, kilometer-scale bathymetric features and associated fine flow patterns remain unresolved by most global predictive systems. For long-term climate simulations, roughness-induced dynamics will remain subgrid in the foreseeable future. This difficulty is further aggravated by the ubiquity of roughness and the lack of high-resolution bathymetric data across vast regions of the seafloor. Given its undeniable significance, parameterizing the impact of roughness on larger scales of motion represents a much-needed improvement for simulations. However, current ocean models treat the interaction between the flow and the bottom boundary in a simplistic, ad hoc manner. Forcing by unresolved bathymetry is combined with other physical processes and represented by linear or quadratic relations between bottom drag and abyssal velocity. Notably, both linear and quadratic drag models were designed to capture vertical momentum transfer by small-scale turbulence in the bottom mixed layer. These relationships may be incompatible with the dynamically dissimilar, and likely stronger, roughness-induced drag (Radko, 2024a).

A promising development in this area is the sandpaper theory of flow-topography interaction—see Radko (2024a, 2024b) and references therein. The model uses conventional techniques of multiscale homogenization theory (e.g., Goldsmith & Esler, 2021; Mei & Vernescu, 2010; Vanneste, 2000, 2003) to formulate evolutionary equations for large-scale flows. The multiscale theories are based on an asymptotic expansion in a small parameter quantifying the scale separation between processes we wish to parameterize and those we intend to resolve. The interaction of processes operating at dissimilar scales is represented by multiple sets of spatial and/or temporal variables. Such models use balances arising at each order in the expansion to formulate solvability conditions that describe the system's evolution entirely on large scales. However, the defining feature of the multiscale sandpaper theory is the focus on the statistical spectral properties of the seafloor relief (Goff, 2020; Goff & Jordan, 1988), which are expected to be more universal than topographic patterns in physical space. Because sandpaper theory is explicit and dynamically transparent, it holds promise to concurrently elucidate key mechanisms at play and offer parameterizations for coarse-resolution models.

While earlier versions of the sandpaper model captured key large-scale effects of roughness (Radko, 2022a, 2022b, 2023a, 2023b), further development is necessary before it can be implemented in comprehensive circulation models. Perhaps the most severe restriction on the model's applicability is posed by the local approximation of topographic forcing. The sandpaper theory is formulated for multilayer isopycnal systems. From the outset, it assumes that roughness can directly influence only the deepest density layer. This assumption is valid for systems in which the bottom layer occupies a significant fraction of the water column. However, the local approximation is questionable when the bottom layer is too shallow to encompass the entire region directly affected by roughness. The schematic in Figure 1 illustrates the principal complication. When layers are sufficiently thin, rough topography perturbs several density interfaces in the abyssal zone, generating small-scale variability in the velocity and layer-thickness fields. In each affected layer, this variability produces the eddy form drag and Reynolds stresses that, in turn, influence larger scales of motion.

Thus, the local sandpaper theory ignores a potentially significant contribution to roughness-induced forcing from layers not directly in contact with the topography. A difficult choice must be made when implementing local parameterization in isopycnal models. Users can either adopt a configuration with an exceedingly deep bottom layer, which permits only a crude representation of stratification, or a priori dismiss potentially important non-local components of topographic forcing. Since neither option is particularly appealing, we now develop a non-local sandpaper theory, in which the effects of roughness are distributed throughout the entire water column. The associated parameterization is implemented in the HYbrid Coordinate Ocean Model (HYCOM)—a generalized vertical-coordinate ocean circulation model used for climate prediction, operational forecasting, and process-oriented studies (Bleck, 2002; Chassignet et al., 2003, 2006, 2009; Metzger et al., 2014). We test the sandpaper closure on the canonical vortex spin-down problem against the corresponding roughness-resolving simulations.

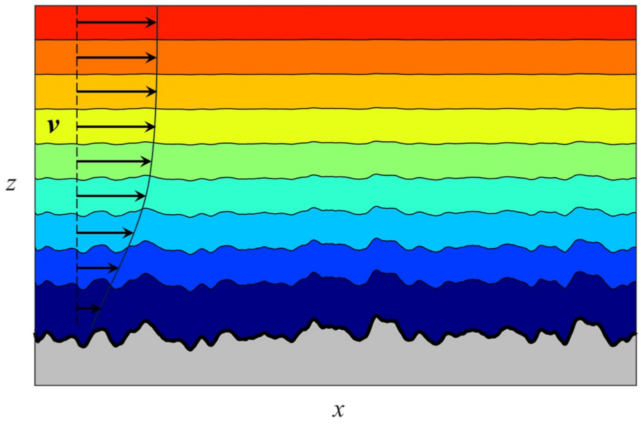

Figure 1. Schematic diagram illustrating the interaction of multilayer flows with rough topography. When the bottom layer thickness is less than the height of the direct influence of roughness, the small-scale variability in seafloor relief perturbs several interfaces in the abyssal zone. This small-scale variability leads to the systematic forcing of larger-scale motions in the affected layers.

The material is organized as follows. The governing multilayer shallow-water equations are presented in Section 2. Section 3 describes the development of the non-local sandpaper theory. In Section 4, the theory-based roughness parameterization is implemented in HYCOM and validated through topography-resolving simulations. The results are summarized, and conclusions are drawn, in Section 5.

2. Formulation

The governing equations are based on the multilayer shallow-water model (e.g., Pedlosky, 1987, Chapter 3):

$$\begin{cases} \dfrac{\partial \boldsymbol{v}_i^*}{\partial t^*} + \left(\boldsymbol{v}_i^* \cdot \nabla\right)\boldsymbol{v}_i^* + \left(-f^* v_i^*, f^* u_i^*\right) = -\dfrac{1}{\rho_0^*}\nabla p_i^* + \upsilon^*\nabla^2\boldsymbol{v}_i^* - \mu^*\nabla^4\boldsymbol{v}_i^* - \delta_{n\,i}\gamma^*\dfrac{\boldsymbol{v}_i^*}{h_i^*} + \delta_{1\,i}\dfrac{\boldsymbol{\tau}^*}{\rho_0^* h_i^*} \\ \dfrac{\partial h_i^*}{\partial t^*} + \nabla\cdot\left(\boldsymbol{v}_i^* h_i^*\right) = 0. \end{cases} \tag{1}$$

The asterisks denote dimensional quantities and $\boldsymbol{v}_i^* = \left(u_i^*, v_i^*\right)$ is the lateral velocity in layer $i = 1,\ldots,n$, where $i = 1$ and $i = n$ represent the surface and bottom layers, respectively. Dynamic pressure is denoted by p_i^*, ρ_0^* is the reference density of the Boussinesq approximation, h_i^* is the thickness of layer i, f^* is the Coriolis parameter, $\delta_{i\,j}$ is the Kronecker delta, $\boldsymbol{\tau}^* = \left(\tau_x^*, \tau_y^*\right)$ is the wind stress, and γ^* is the bottom drag coefficient. The lateral dissipation of momentum in mainstream ocean models, including HYCOM, is represented by a combination of Laplacian (υ^*) and bi-harmonic (μ^*) eddy viscosities. The shallow-water model also assumes the hydrostatic balance, which connects the dynamic pressure in adjacent layers:

$$p_i^* = p_{i+1}^* + g^*\left(\rho_{i+1}^* - \rho_i^*\right)\sum_{j=1}^{i} h_j^*, \quad i = 1,\ldots,n-1. \tag{2}$$

The number of controlling parameters is reduced by non-dimensionalizing the governing equations as follows:

$$\boldsymbol{v}_i^* = f_0^* L^* \boldsymbol{v}_i, \quad p_i^* = \rho_0^*\left(f_0^* L^*\right)^2 p_i, \quad \left(x^*, y^*\right) = L^*(x, y), \quad t^* = \frac{t}{f_0^*}, \quad h_i^* = H_0^* h_i, \tag{3}$$

where L^*, H_0^*, and f_0^* are the representative scales for the width of small-scale topographic features, vertical extent of the model, and the Coriolis parameter, respectively.

The non-dimensional momentum and thickness equations take the form

$$\begin{cases} \dfrac{\partial \boldsymbol{v}_i}{\partial t} + (\boldsymbol{v}_i \cdot \nabla)\,\boldsymbol{v}_i + (-f v_i, f u_i) = -\nabla p_i + \upsilon \nabla^2 \boldsymbol{v}_i - \mu \nabla^4 \boldsymbol{v}_i - \delta_{n\,i}\,\gamma \dfrac{\boldsymbol{v}_i}{h_i} + \delta_{1\,i} \dfrac{\boldsymbol{\tau}}{h_i} \\ \dfrac{\partial h_i}{\partial t} + \nabla \cdot (\boldsymbol{v}_i h_i) = 0, \end{cases} \quad i = 1, \dots, n \tag{4}$$

where

$$\boldsymbol{\tau} = \frac{\boldsymbol{\tau}^*}{\rho_0^* L^* f_0^{*2} H_0^*}, \quad \upsilon = \frac{\upsilon^*}{L^{*2} f_0^*}, \quad \mu = \frac{\mu^*}{L^{*4} f_0^*}, \quad \gamma = \frac{\gamma^*}{f_0^* H_0^*}. \tag{5}$$

The recursive relation (Equation 2) reduces in non-dimensional units to

$$p_i = p_{i+1} + B_{i,i+1} \sum_{j=1}^{i} h_j^*, \quad i = 1, \dots, n-1, \tag{6}$$

where $B_{i,i+1} = \frac{g^*\left(\rho_{i+1}^* - \rho_i^*\right) H_0^*}{\rho_0^* \left(f_0^* L^*\right)^2}$ is the Burger number.

The development of the sandpaper theory centers on the potential vorticity (PV) equation. It is obtained by taking the curl of the momentum equations (Equation 4), which eliminates the pressure gradient terms, and combining it with the thickness equation:

$$\frac{\partial q_i}{\partial t} + u_i \frac{\partial q_i}{\partial x} + v_i \frac{\partial q_i}{\partial y} = F_{q\,i}. \tag{7}$$

The relative and potential vorticities are denoted as $\varsigma_i = \frac{\partial v_i}{\partial x} - \frac{\partial u_i}{\partial y}$ and $q_i = \frac{f + \varsigma_i}{h_i}$, respectively. Quantity $F_{q\,i}$ on the right-hand side of Equation 7 represents processes affecting the Lagrangian conservation of PV:

$$F_{q\,i} = \upsilon \frac{\nabla^2 \varsigma_i}{h_i} - \mu \frac{\nabla^4 \varsigma_i}{h_i} - \delta_{n\,i} \frac{\gamma}{h_n} \nabla \times \left(\frac{\boldsymbol{v}_n}{h_n}\right) + \delta_{1\,i} \nabla \times \left(\frac{\boldsymbol{\tau}}{h_1}\right). \tag{8}$$

To perform the asymptotic multiscale analysis, we introduce the scale-separation parameter

$$\varepsilon = \sqrt{\frac{L^*}{L_{LS}^*}} = \frac{1}{\sqrt{L_{LS}}} \ll 1, \tag{9}$$

where L_{LS}^* is the representative dimensional lateral extent of the large-scale flow, and L_{LS} is its non-dimensional counterpart. This parameter defines the new set of spatial scales (X, Y) that reflect the dynamics of large-scale processes, which are related to the original ones as follows:

$$(X, Y) = \varepsilon^2 (x, y). \tag{10}$$

The derivatives in the governing equations are replaced accordingly:

$$\frac{\partial}{\partial x} \to \frac{\partial}{\partial x} + \varepsilon^2 \frac{\partial}{\partial X}, \quad \frac{\partial}{\partial y} \to \frac{\partial}{\partial y} + \varepsilon^2 \frac{\partial}{\partial Y}. \tag{11}$$

The elevation of the seafloor relative to its global mean level is denoted as $\eta = 1 - H$, where H is the total ocean depth relative to the still-water level. In the commonly used rigid lid approximation, H is equal to the sum of individual layer thicknesses:

$$\sum_{i=1}^{n} h_i = H = 1 - \eta. \tag{12}$$

We assume that the seafloor elevation varies on both large and small scales. To isolate its large-scale (η_L) and small-scale (η_S) components, η is written as

$$\eta = \eta_L(X, Y) + \eta_S(X, Y, x, y), \tag{13}$$

where

$$\eta_L = \langle \eta \rangle, \quad \eta_S = \eta'. \tag{14}$$

The angle brackets represent averaging over small-scale variables, and primes denote the deviation from the mean: $a' \equiv a - \langle a \rangle$.

The subsequent developments also make use of the Parseval identity (Parseval, 1806):

$$\langle ab \rangle = \iint \tilde{a} \cdot \mathrm{conj}\left(\tilde{b}\right) dk\, dl, \tag{15}$$

where tildes denote Fourier images and (k, l) are the (x,y) wavenumbers of small-scale patterns. The Fourier transform is defined as follows:

$$a = \frac{\sqrt{L_x L_y}}{2\pi} \iint \tilde{a}(k, l) \exp(Ikx + Ily)\, dk\, dl, \tag{16}$$

where (L_x, L_y) is the domain size and $I \equiv \sqrt{-1}$. The sandpaper model considers statistically isotropic small-scale components of bathymetry and therefore

$$\left|\tilde{\eta}_S\right|^2 = F_\eta(X, Y, \kappa), \tag{17}$$

where $\kappa \equiv \sqrt{k^2 + l^2}$.

3. The Multiscale Analysis

3.1. Fast Flows

The non-local sandpaper model utilizes standard methods of multiscale mechanics (e.g., Mei & Vernescu, 2010). The analysis is focused on the asymptotic sector with representative velocity $U = O(\varepsilon)$ and $\upsilon = O(\varepsilon^2)$. This regime is characterized by asymptotically large Reynolds numbers $\mathrm{Re} = \frac{L^* U^*}{\upsilon^*} = O(\varepsilon^{-1})$, and the solutions obtained for this sector will be referred to as the fast-flow model. The system evolves on two distinct temporal scales—advective and roughness-induced. Since non-dimensional large spatial scales are $L_{LS} = O(\varepsilon^{-2})$, whereas the non-dimensional large-scale velocity is $O(\varepsilon)$, the advective timescale is represented by the variable $T_3 = \varepsilon^3 t$. However, as will be seen shortly, rough topography affects the flow field over longer timescales: $T_4 = \varepsilon^4 t$. Thus, the time derivatives in the governing equations are replaced by

$$\frac{\partial}{\partial t} \rightarrow \varepsilon^3 \frac{\partial}{\partial T_3} + \varepsilon^4 \frac{\partial}{\partial T_4}. \tag{18}$$

The Coriolis parameter is uniquely determined by the large-scale meridional coordinate $f = f(Y)$, while the forcing and dissipative parameters are rescaled as follows:

$$(\upsilon, \mu, \gamma, \boldsymbol{\tau}) = \varepsilon^2 (\upsilon_0, \mu_0, \gamma_0, \boldsymbol{\tau}_0). \tag{19}$$

The expansion opens with the $O(\varepsilon)$ large-scale velocity field in each layer ($i = 1,\dots,n$):

$$\mathbf{v}_i = \varepsilon \mathbf{v}_i^{(1)}(X,Y,T_3,T_4) + \sum_{j=2}^{\infty} \varepsilon^j \mathbf{v}_i^{(j)}(X,Y,x,y,T_3,T_4). \tag{20}$$

The corresponding pressure field takes the form

$$p_i = \varepsilon^{-1} p_i^{(-1)}(X,Y,T_3,T_4) + p_i^{(0)}(X,Y,T_3,T_4) + \varepsilon p_i^{(1)}(X,Y,T_3,T_4) + \sum_{j=2}^{\infty} \varepsilon^j p_i^{(j)}(X,Y,x,y,T_3,T_4), \tag{21}$$

and the analogous notation is used for the PV series. The Burger number in the recursive relation (Equation 6) is based on the roughness length-scale ($L^* \sim 10$ km), which is comparable to the radius of deformation in the abyssal ocean. Thus, $B_{i,i+1}$ is considered an $O(1)$ quantity. The small-scale bathymetric variability is weak:

$$\eta_S = \varepsilon^2 \eta_{S0}, \tag{22}$$

and the solution for the thickness is sought in terms of a power series

$$h_i = h_i^{(0)}(X,Y,T_3,T_4) + \varepsilon h_i^{(1)}(X,Y,T_3,T_4) + \sum_{j=2}^{\infty} \varepsilon^j h_i^{(j)}(X,Y,x,y,T_3,T_4). \tag{23}$$

The series for (u_i, v_i, h_i) are substituted into the governing equations, and terms of the same order are combined. The analysis commences by considering the leading-order perturbation balances. In the PV equation (Equation 7), the small-scale components emerge first at $O(\varepsilon^3)$:

$$\frac{\partial q_i^{(0)}}{\partial T_3} + u_i^{(1)} \frac{\partial q_i^{(2)}}{\partial x} + v_i^{(1)} \frac{\partial q_i^{(2)}}{\partial y} + u_i^{(1)} \frac{\partial q_i^{(0)}}{\partial X} + v_i^{(1)} \frac{\partial q_i^{(0)}}{\partial Y} = 0, \tag{24}$$

where $q_i^{(0)} = \frac{f}{h_i^{(0)}}$, and

$$q_i^{(2)} = \frac{1}{h_i^{(0)}} \left(\frac{\partial v_i^{(2)}}{\partial x} + \frac{\partial v_i^{(0)}}{\partial X} - \frac{\partial u_i^{(2)}}{\partial y} - \frac{\partial u_i^{(0)}}{\partial Y} - h_i^{(1)} q_i^{(1)} - h_i^{(2)} q_i^{(0)} \right). \tag{25}$$

We form the perturbation equations by subtracting the full equations and their (x, y) averages. For Equation 24, we arrive at

$$u_i^{(1)} \frac{\partial {q'}_i^{(2)}}{\partial x} + v_i^{(1)} \frac{\partial {q'}_i^{(2)}}{\partial y} = 0, \tag{26}$$

whereas for Equation 25 we obtain

$${q'}_i^{(2)} = \frac{1}{h_i^{(0)}} \left(\frac{\partial {v'}_i^{(2)}}{\partial x} - \frac{\partial {u'}_i^{(2)}}{\partial y} - {h'}_i^{(2)} q_i^{(0)} \right). \tag{27}$$

If we restrict the analysis to well-behaved patterns of ${q'}_i^{(2)}$ with continuous small-scale spectra (Equation 26), demands that ${q'}_i^{(2)} = 0$. This feature reflects the tendency toward homogenization of PV (e.g., Dewar, 1986; Marshall et al., 1999; Pudig & Smith, 2025; Radko, 2022a, 2022b; Rhines & Young, 1982). PV-homogenization reduces (Equation 27) to

$$\frac{\partial {v'}_i^{(2)}}{\partial x} - \frac{\partial {u'}_i^{(2)}}{\partial y} - \frac{f {h'}_i^{(2)}}{h_i^{(0)}} = 0. \tag{28}$$

The $O(\varepsilon^4)$ PV balance is treated in a similar manner, which yields

$$u_i^{(1)}\frac{\partial q'^{(3)}_i}{\partial x} + v_i^{(1)}\frac{\partial q'^{(3)}_i}{\partial y} = -u'^{(2)}_i\frac{\partial q_i^{(0)}}{\partial X} - v'^{(2)}_i\frac{\partial q_i^{(0)}}{\partial Y} + \frac{\upsilon_0}{h_i^{(0)}}\nabla^2\varsigma'^{(2)}_i - \frac{\mu_0}{h_i^{(0)}}\nabla^4\varsigma'^{(2)}_i - \delta_{n\,i}\frac{\gamma_0}{h_i^{(0)2}}\varsigma'^{(2)}_i, \tag{29}$$

where

$$q'^{(3)}_i = \frac{1}{h_i^{(0)}}\left(\frac{\partial v'^{(3)}_i}{\partial x} + \frac{\partial v'^{(3)}_i}{\partial X} - \frac{\partial u'^{(3)}_i}{\partial y} - \frac{\partial u'^{(3)}_i}{\partial Y} - h'^{(2)}_i q_i^{(1)} - h'^{(3)}_i q_i^{(0)}\right). \tag{30}$$

The leading order perturbation momentum equations are

$$\begin{cases} f v'^{(2)}_i = \dfrac{\partial p'^{(2)}_i}{\partial x} \\ f u'^{(2)}_i = -\dfrac{\partial p'^{(2)}_i}{\partial y}. \end{cases} \tag{31}$$

The leading-order small-scale balances representing PV-homogenization (Equation 28) and geostrophic approximation (Equation 31) are used to connect the perturbation pressure and thickness:

$$\nabla^2 p'^{(2)}_i = \frac{f^2 h'^{(2)}_i}{h_i^{(0)}}, \tag{32}$$

which, in turn, yields the velocity components

$$\begin{cases} \nabla^2 u'^{(2)}_i = -\dfrac{f}{h_i^{(0)}}\dfrac{\partial h'^{(2)}_i}{\partial y} \\ \nabla^2 v'^{(2)}_i = \dfrac{f}{h_i^{(0)}}\dfrac{\partial h'^{(2)}_i}{\partial x}. \end{cases} \tag{33}$$

The leading-order small-scale component of the recursive relation (Equation 6) takes the form

$$p'^{(2)}_i = p'^{(2)}_{i+1} + B_{i,i+1}\sum_{j=1}^{i} h'^{(2)}_j. \tag{34}$$

We also use Equation 12, which states that the sum of all layer thicknesses equals the total depth. Since this relation is linear, we readily isolate its small-scale second-order component:

$$\sum_{i=1}^{n} h'^{(2)}_i = -\eta_{S0}, \tag{35}$$

which implies that the sum of small-scale layer-thickness perturbations equals the small-scale component of the ocean depth. The system (Equations 32, 34 and 35) represents a closed set of linear equations that can be used to infer the pattern of the small-scale thickness $h'^{(2)}_i$ from $h_i^{(0)}$ and η_{S0}. We Fourier-transform this system in small-scale variables (x,y) and eliminate $\tilde{p}'^{(2)}_i$, which results in

$$\begin{cases} \dfrac{f^2 a_i}{\kappa^2 h_i^{(0)}} - \dfrac{f^2 a_{i+1}}{\kappa^2 h_{i+1}^{(0)}} + B_{i,i+1} \displaystyle\sum_{j=1}^{i} a_j = 0, i = 1, \ldots, n-1 \\ \displaystyle\sum_{i=1}^{n} a_i = 1, \end{cases} \tag{36}$$

where a_i is the small-scale thickness component normalized by the seafloor roughness:

$$a_i = -\frac{\widetilde{h'}_i^{(2)}}{\tilde{\eta}_{S0}}. \tag{37}$$

Equation 36 makes it possible to determine, for any given large-scale stratification, the distribution of small-scale perturbations throughout the water column. The array a_i represents the vertical attenuation of small-scale topographic signatures. The local model (Radko, 2024b) assumes that the effects of seafloor roughness are limited to the lowest layer, which is equivalent to assigning $a_i = \delta_{n\ i}$. In contrast, the present formulation permits finite values of a_i in all layers, making it possible to explore the non-local large-scale effects of seafloor roughness. In this study, we consider isotropic patterns of bottom roughness (Equation 17). Thus, Equations 36 and 37 imply that small-scale patterns of attenuation coefficients are isotropic: $a_i = a_i(X, Y, T_3, T_4, \kappa)$. This, in turn, indicates that small-scale thickness and pressure patterns are also statistically isotropic.

Having determined the leading-order perturbation components, we now proceed to formulate large-scale equations. To that end, we average the governing system in x and y, focusing on the transfer of momentum and density by small-scale eddies. Our goal is to identify the leading-order components of roughness-induced forcing. Considering Equations 31 and 32, we conclude that

$$\left\langle u'^{(2)}_i \frac{\partial u'^{(2)}_i}{\partial x} \right\rangle = \left\langle v'^{(2)}_i \frac{\partial u'^{(2)}_i}{\partial y} \right\rangle = \left\langle u'^{(2)}_i \frac{\partial v'^{(2)}_i}{\partial x} \right\rangle = \left\langle v'^{(2)}_i \frac{\partial v'^{(2)}_i}{\partial y} \right\rangle = \left\langle u'^{(2)}_i h'^{(2)}_i \right\rangle = \left\langle v'^{(2)}_i h'^{(2)}_i \right\rangle = 0. \tag{38}$$

Thus, the small-scale eddy forcing terms emerge first at $O(\varepsilon^5)$ in the momentum equations and $O(\varepsilon^7)$ in the thickness equation. The mean fifth-order momentum equation takes the form

$$\frac{\partial \left\langle \boldsymbol{v}_i^{(2)} \right\rangle}{\partial T_3} + \frac{\partial \boldsymbol{v}_i^{(1)}}{\partial T_4} + \boldsymbol{A}_i^{(5)} + \boldsymbol{R}_i^{(5)} + \left(-f \left\langle v_i^{(5)} \right\rangle, f \left\langle u_i^{(5)} \right\rangle \right) = -\nabla_{\boldsymbol{X}} \left\langle p_i^{(3)} \right\rangle - \delta_{n\ i} \gamma_0 \frac{\left\langle \boldsymbol{v}_n^{(3)} \right\rangle}{h_n^{(0)}}, \tag{39}$$

where $\nabla_{\boldsymbol{X}} \equiv \left(\frac{\partial}{\partial X}, \frac{\partial}{\partial Y} \right)$ denotes the large-scale gradient, and $\boldsymbol{A}_i^{(5)} = \left(A_{x\ i}^{(5)}, A_{y\ i}^{(5)} \right)$ is the mean-field advection:

$$\begin{cases} A_{x\ i}^{(5)} = \boldsymbol{v}_i^{(1)} \cdot \nabla_{\boldsymbol{X}} \left\langle u_i^{(2)} \right\rangle + \left\langle \boldsymbol{v}_i^{(2)} \right\rangle \cdot \nabla_{\boldsymbol{X}} u_i^{(1)} \\ A_{y\ i}^{(5)} = \boldsymbol{v}_i^{(1)} \cdot \nabla_{\boldsymbol{X}} \left\langle v_i^{(2)} \right\rangle + \left\langle \boldsymbol{v}_i^{(2)} \right\rangle \cdot \nabla_{\boldsymbol{X}} v_i^{(1)} \end{cases}. \tag{40}$$

Term $\boldsymbol{R}_i^{(5)} = \left(R_{x\ i}^{(5)}, R_{y\ i}^{(5)} \right)$ represents the Reynolds stresses:

$$\begin{cases} R_{x\ i}^{(5)} = \left\langle \boldsymbol{v}'^{(2)}_i \cdot \nabla u'^{(3)}_i \right\rangle + \left\langle \boldsymbol{v}'^{(3)}_i \cdot \nabla u'^{(2)}_i \right\rangle \\ R_{y\ i}^{(5)} = \left\langle \boldsymbol{v}'^{(2)}_i \cdot \nabla v'^{(3)}_i \right\rangle + \left\langle \boldsymbol{v}'^{(3)}_i \cdot \nabla v'^{(2)}_i \right\rangle. \end{cases} \tag{41}$$

In the thickness equation, the roughness-induced eddy forcing appears first at $O(\varepsilon^7)$:

$$\frac{\partial\left\langle h_i^{(4)}\right\rangle}{\partial T_3}+\frac{\partial\left\langle h_i^{(3)}\right\rangle}{\partial T_4}+\frac{\partial}{\partial X}\left(\sum_{j=1}^{5}\left\langle u_i^{(j)}\right\rangle\left\langle h_i^{(5-j)}\right\rangle+\left\langle u'^{(2)}_i h'^{(3)}_i\right\rangle+\left\langle u'^{(3)}_i h'^{(2)}_i\right\rangle\right)$$
$$+\frac{\partial}{\partial Y}\left(\sum_{j=1}^{5}\left\langle v_i^{(j)}\right\rangle\left\langle h_i^{(5-j)}\right\rangle+\left\langle v'^{(2)}_i h'^{(3)}_i\right\rangle+\left\langle v'^{(3)}_i h'^{(2)}_i\right\rangle\right)=0, \tag{42}$$

where it is represented by terms $\left\langle \boldsymbol{v}'^{(2)}_i h'^{(3)}_i\right\rangle$ and $\left\langle \boldsymbol{v}'^{(3)}_i h'^{(2)}_i\right\rangle$. These eddy-transfer components are treated using the Transformed Eulerian Mean framework (e.g., Andrews & Mcintyre, 1976), which reformulates governing equations in terms of residual circulation. The result of this transformation is a system in which small-scale forcing appears exclusively in the momentum equations, leading to several conceptual and technical simplifications. In the present context, the residual velocities take the form

$$\boldsymbol{v}_{res\ i}=\left\langle \boldsymbol{v}_i^{(5)}\right\rangle+\frac{\left\langle \boldsymbol{v}'^{(2)}_i h'^{(3)}_i\right\rangle+\left\langle \boldsymbol{v}'^{(3)}_i h'^{(2)}_i\right\rangle}{h_i^{(0)}}. \tag{43}$$

We now use Equation 43 to express the momentum equations (Equation 39) in terms of residual, rather than mean velocities:

$$\frac{\partial\left\langle \boldsymbol{v}_i^{(2)}\right\rangle}{\partial T_3}+\frac{\partial \boldsymbol{v}_i^{(1)}}{\partial T_4}+\boldsymbol{A}_i^{(5)}+\left(-f v_{res\ i}, f u_{res\ i}\right)=-\nabla_{\boldsymbol{X}}\left\langle p_i^{(3)}\right\rangle-\delta_{n\ i}\gamma_0\frac{\left\langle \boldsymbol{v}_n^{(3)}\right\rangle}{h_n^{(0)}}+\boldsymbol{D}_i^{(5)}, \tag{44}$$

where $\boldsymbol{D}_i^{(5)}=\left(D_{x\ i}^{(5)}, D_{y\ i}^{(5)}\right)$ represents small-scale momentum forcing:

$$\begin{cases} D_{x\ i}^{(5)}=-R_{x\ i}^{(5)}-q_i^{(0)}\left\langle v'^{(2)}_i h'^{(3)}_i\right\rangle-q_i^{(0)}\left\langle v'^{(3)}_i h'^{(2)}_i\right\rangle \\ D_{y\ i}^{(5)}=-R_{y\ i}^{(5)}+q_i^{(0)}\left\langle u'^{(2)}_i h'^{(3)}_i\right\rangle+q_i^{(0)}\left\langle u'^{(3)}_i h'^{(2)}_i\right\rangle. \end{cases} \tag{45}$$

These expressions can be further simplified by combining Equations 25, and 30, and 41:

$$\begin{cases} D_{x\ i}^{(5)}=h_i^{(0)}\left\langle v'^{(2)}_i q'^{(3)}_i\right\rangle \\ D_{y\ i}^{(5)}=-h_i^{(0)}\left\langle u_i^{(2)} q'^{(3)}_i\right\rangle. \end{cases} \tag{46}$$

To complete the development of the model, it is necessary to express the PV fluxes $\boldsymbol{R}_{q\ i}=h_i^{(0)}\left\langle \boldsymbol{v}'^{(2)}_i q'^{(3)}_i\right\rangle$ in terms of large-scale properties. To that end, we turn to the fourth-order PV equation (Equation 29). Following Radko (2024b), we perform the analysis in the Fourier space and evaluate $\boldsymbol{R}_{q\ i}$ using the Parseval identity (Equation 15):

$$\left\langle \boldsymbol{v}'^{(2)}_i q'^{(3)}_i\right\rangle=\iint \widetilde{\boldsymbol{v}'}^{(2)}_i\cdot\mathrm{conj}\left(\widetilde{q'}^{(3)}_i\right)dk\,dl. \tag{47}$$

Since the PV equation (Equation 29) provides only the along-flow variation in $q'^{(3)}_i$, we adopt the flow-following coordinate system

$$\begin{cases} \hat{k}=k\cos\theta_i+l\sin\theta_i \\ \hat{l}=-k\sin\theta_i+l\cos\theta_i \end{cases}, \tag{48}$$

where the flow-orientation variable θ_i is defined by

$$\cos(\theta_i) = \frac{u_i^{(1)}}{\left|\boldsymbol{v}_i^{(1)}\right|}, \quad \sin(\theta_i) = \frac{v_i^{(1)}}{\left|\boldsymbol{v}_i^{(1)}\right|}. \tag{49}$$

In the flow-following coordinate system, the Fourier image of Equation 29 reduces to

$$\left|\boldsymbol{v}_i^{(1)}\right| \ I\ \hat{k}\ \tilde{q}'^{(3)}_i = -\widetilde{u'}^{(2)}_i \frac{\partial q_i^{(0)}}{\partial X} - \widetilde{v'}^{(2)}_i \frac{\partial q_i^{(0)}}{\partial Y} - \frac{\upsilon_0}{h_i^{(0)}} \kappa^2 \widetilde{\varsigma'}^{(2)}_i - \frac{\mu_0}{h_i^{(0)}} \kappa^4 \widetilde{\varsigma'}^{(2)}_i - \frac{\delta_{n\ i}\,\gamma_0}{h_i^{(0)2}} \widetilde{\varsigma'}^{(2)}_i, \tag{50}$$

which is further simplified using Equation 33:

$$\tilde{q}'^{(3)}_i = \frac{1}{\left|\boldsymbol{v}_i^{(1)}\right| \ I\ \hat{k}} \left(-\frac{f\ I\ l\ \tilde{h}_i^{(2)}}{h_i^{(0)} \kappa^2} \frac{\partial q_i^{(0)}}{\partial X} + \frac{f\ I\ k\ \tilde{h}_i^{(2)}}{h_i^{(0)} \kappa^2} \frac{\partial q_i^{(0)}}{\partial Y} - \frac{f\ \ \tilde{h}_i^{(2)}}{h_i^{(0)2}} \left[\upsilon_0 \kappa^2 + \mu_0 \kappa^4 + \frac{\delta_{n\ i} \gamma_0}{h_i^{(0)}} \right] \right). \tag{51}$$

This expression is then used to evaluate Equation 47 and thereby determine $\boldsymbol{R}_{q\ i}$:

$$\begin{cases} h_i^{(0)} \left\langle u'^{(2)}_i q'^{(3)}_i \right\rangle = \dfrac{2\pi f^2}{\left|\boldsymbol{v}_i^{(1)}\right| h_i^{(0)2}} \sin\theta \displaystyle\int \left(\upsilon_0 \kappa + \mu_0 \kappa^3 + \frac{\delta_{n\ i} \gamma_0}{h_i^{(0)} \kappa} \right) \left| h'^{(2)}_i \right|^2 d\kappa \\ h_i^{(0)} \left\langle v'^{(2)}_i q'^{(3)}_i \right\rangle = -\dfrac{2\pi f^2}{\left|\boldsymbol{v}_i^{(1)}\right| h_i^{(0)2}} \cos\theta \displaystyle\int \left(\upsilon_0 \kappa + \mu_0 \kappa^3 + \frac{\delta_{n\ i} \gamma_0}{h_i^{(0)} \kappa} \right) \left| h'^{(2)}_i \right|^2 d\kappa. \end{cases} \tag{52}$$

The multiscale analysis is now complete, and we rewrite the evolutionary large-scale equations for the bottom layer using the original independent variables (x,y,t) in place of (X,Y,T). The entire set of evolutionary large-scale equations is reconstructed by combining all (x,y)-averaged balances. The result is simplified by introducing the large-scale field variables

$$\overline{\boldsymbol{v}}_i = \sum_{j=1}^{4} \varepsilon^j \left\langle \boldsymbol{v}_i^{(j)} \right\rangle + \varepsilon^5 \boldsymbol{v}_{res}, \quad \overline{h}_i = \sum_{j=0}^{4} \varepsilon^j \left\langle h_i^{(j)} \right\rangle, \quad \overline{p}_i = \sum_{j=-1}^{3} \varepsilon^j \left\langle p_i^{(j)} \right\rangle, \tag{53}$$

which leads to

$$\begin{cases} \dfrac{\partial \overline{\boldsymbol{v}}_i}{\partial t} + (\overline{\boldsymbol{v}}_i \cdot \nabla)\, \overline{\boldsymbol{v}}_i + (-f \overline{v}_i, f \overline{u}_i) = -\nabla \overline{p}_i + \upsilon \nabla^2 \overline{\boldsymbol{v}}_i - \mu \nabla^4 \overline{\boldsymbol{v}}_i - \delta_{n\,i}\, \gamma \dfrac{\overline{\boldsymbol{v}}_i}{h_i} + \delta_{1\,i}\ \dfrac{\boldsymbol{\tau}}{h_i} + \boldsymbol{D}_i^{(\text{fast})} \\ \dfrac{\partial \overline{h}_i}{\partial t} + \nabla \cdot \left(\overline{\boldsymbol{v}}_i \overline{h}_i \right) = 0, \end{cases} \tag{54}$$

where $\boldsymbol{D}_i^{(\text{fast})}$ is the roughness-induced drag:

$$\boldsymbol{D}_i^{(fast)} = \varepsilon^5 \boldsymbol{D}_i^{(5)} = -\frac{2\pi f^2}{\overline{h}_i^2} \frac{\overline{\boldsymbol{v}}_i}{|\overline{\boldsymbol{v}}_i|^2} \int a_i^2 \left(\upsilon\kappa + \mu\kappa^3 + \frac{\delta_{n\ i}\gamma}{\overline{h}_i \kappa} \right) |\eta_S|^2 d\kappa. \tag{55}$$

In deriving Equation 54, we have neglected $o\left(\varepsilon^5\right)$ terms in the momentum equations and $o\left(\varepsilon^7\right)$ terms in the thickness equation. Thus, the explicit viscous terms $\upsilon \nabla^2 \boldsymbol{v}_i \sim O\left(\varepsilon^7\right)$ and $\mu \nabla^4 \boldsymbol{v}_i \sim O\left(\varepsilon^{11}\right)$ could have been neglected. However, they are retained in Equation 54 to maintain the structural similarity with the governing equations (Equation 4). Their inclusion does not affect the asymptotic accuracy of the large-scale model.

The expression (Equation 55) is analogous to the forcing patterns in the local model (Radko, 2024b). The key difference is that the roughness signal is now distributed through the entire water column. This signal is modulated by the attenuation factors a_i, which can be readily obtained for a given stratification pattern using Equation 36. It should be emphasized that the attenuation factors a_i become vanishingly small in the limit of $\bar{h}_i \rightarrow 0$. This feature has far-reaching consequences for implementing the sandpaper parameterization in numerical isopycnal models. In realistic configurations, density interfaces often intersect the seafloor, and the bottom layer depth in such locations approaches zero $\left(\bar{h}_n \rightarrow 0\right)$. In this limit, the roughness-induced forcing predicted by the local model increases without bound $\left(|\boldsymbol{D}_{\text{loc}}| \propto \bar{h}_n^{-2}\right)$. In contrast, the non-local model remains well-behaved and physical. To highlight this property, we express the foregoing formulation in terms of the normalized attenuation factors $b_i = \frac{a_i}{\bar{h}_i}$, which reduces Equation 55 to

$$\boldsymbol{D}_i^{(\text{fast})} = -2\pi f^2 \frac{\bar{\boldsymbol{v}}_i}{|\bar{\boldsymbol{v}}_i|^2} \int b_i^2 \left(\upsilon\kappa + \mu\kappa^3 + \frac{\delta_{n\ i}\gamma}{\bar{h}_i\kappa}\right) |\eta_S|^2 \kappa d\kappa. \tag{56}$$

The attenuation model (Equation 36) takes the form

$$\begin{cases} f^2(b_i - b_{i+1}) + \kappa^2 B_{i,i+1} \sum\limits_{j=1}^{i} \bar{h}_j b_j = 0, i = 1, \ldots, n-1 \\ \sum\limits_{i=1}^{n} \bar{h}_i b_i = 1. \end{cases} \tag{57}$$

3.2. Interpretation

The non-local model's ability to consistently represent the thin-layer regime is a major step forward relative to its antecedents. However, this advancement also prompts discussion of the essential physics that the non-local model captures, but its local counterpart does not. In this regard, we note that the local sandpaper model (Radko, 2024b) can be readily recovered by assigning the attenuation factors in Equation 57 values of $b_i = \frac{\delta_{n\ i}}{\bar{h}_i}$. The regularity of the non-local solutions (Equation 57) in the limit of $\bar{h}_n \rightarrow 0$ stands in stark contrast to the unphysically singular pattern of the bottom attenuation coefficient $b_n = \frac{1}{\bar{h}_n}$ in the local model. This observation also provides insight into the key dynamic differences between the two systems. In the local model, small-scale variability in thickness is restricted to the bottom layer and therefore $h_n' = -\eta_S$. Thus, when the bottom layer shrinks $\left(\bar{h}_n \rightarrow 0\right)$, perturbation velocities (Equation 33) unphysically increase without bound. This, in turn, leads to a singular behavior of the form drag and Reynolds stresses in the thin-layer limit. The non-local model, on the other hand, permits the penetration of the roughness-induced eddies into the layers above. The leakage of small-scale variability from the bottom layer reduces h_n' and thereby redistributes roughness-induced drag across several layers. Accounting for this effect removes the singularity of the local model.

Another feature of the sandpaper theory that requires clarification is the sensitivity of the roughness-induced forcing (Equation 56) to the assumed dissipation parameters (υ, μ, γ). These parameters themselves represent parameterizations of subgrid processes. In general circulation models, the selection of the momentum transfer coefficients is often affected by numerical stability considerations. However, explicit friction (Laplacian, biharmonic, and Ekman) is introduced in the sandpaper theory to capture dissipative phenomena operating at sub-roughness scales ($L \lesssim 1$ km). These frictional processes perturb the leading-order geostrophic balance of the roughness-induced pattern, resulting in finite eddy form drag and Reynolds stresses. Therefore, we urge caution in selecting relevant values of dissipation parameters in Equation 56. Particularly perilous are circulation models that resolve active turbulence on sub-roughness scales. The momentum transfer by sub-roughness eddies partially replaces the explicit dissipation in coarser simulations. Thus, the sandpaper parameters should be adjusted accordingly. A promising path forward in this area would be the development of roughness-induced drag laws for the hard turbulence limit, in which explicit friction parameters become inconsequential. Another option for future efforts is to leverage the flexibility of the sandpaper model, which enables straightforward adoption of more advanced dissipation closures once they become widely available and accepted by the ocean modeling community.

Fortunately, for many applications, the issue of sub-roughness eddy transfer does not arise. The case in point is the present-day basin-scale simulations, which are performed at lateral resolutions of 1–2 km at best. The maximum gradient spectrum in the Goff-Jordan roughness model peaks at the wavelength of $L_{GJ} \approx 6$ km. Therefore, the sub-roughness eddies in basin-scale models are currently unresolved, and momentum transfer at kilometer scales is controlled by explicit friction. Nevertheless, it is now clear that accounting for the roughness effects is beneficial for large-scale modeling. Several studies (Chassignet & Xu, 2021; Chassignet et al., 2023; Richet et al., 2025) demonstrated that simulations can be brought into closer agreement with observations simply by improving the representation of small-scale topography. However, bathymetry at kilometer scales remains unmapped over most regions of the World Ocean, and roughness-resolving simulations often incur prohibitive computational costs. These complications can be mitigated by incorporating sandpaper closure in global and basin-scale models. In such systems, a reasonable approach would be to implement sandpaper parameterization using the nominal explicit dissipation parameters assumed by general circulation models.

3.3. Regularization

The large-scale model in Equations 54, 56 and 57 represents a closed system of evolutionary equations that captures flow forcing by rough topography. However, there is one physically suspicious and computationally inconvenient feature of this set—the singularity of the forcing term in the limit of weak velocities $|\overline{\boldsymbol{v}}_i| \to 0$. The origin of this singularity lies in the high-Reynolds-number assumption used in the large-scale model. To regularize the limit $|\overline{\boldsymbol{v}}_i| \to 0$, we consider a strongly dissipative system with $\mathrm{Re} \ll 1$ and then develop a hybrid model that captures the transition between fast-flow and slow-flow models. While most of the ocean can be modeled as a high-Re system, regularization prevents parametric simulations from failing near stagnation points where currents effectively stop. The slow-flow model is described in Appendix A. The key result is the topographic forcing function $\boldsymbol{D}_i^{(\mathrm{slow})}$ that replaces $\boldsymbol{D}_i^{(\mathrm{fast})}$ in Equation 54 for weak velocities:

$$\boldsymbol{D}_i^{(\mathrm{slow})} = -\delta_{n\ i} G^{(\mathrm{slow})}\, \overline{\boldsymbol{v}}_i, \tag{58}$$

where the expression for $G^{(\mathrm{slow})}$ in terms of seafloor properties is given in Equation A17. In contrast to the fast-flow model (Equation 56), the forcing function $\boldsymbol{D}_i^{(\mathrm{slow})}$ is well-behaved in the limit $|\overline{\boldsymbol{v}}_i| \to 0$, which enables regularizing the sandpaper parameterization. We also note that the proposed non-monotonic pattern of roughness-induced drag, which increases with flow speed in slow currents and decreases in swift flows, is a robust and generic property. It is borne out in all versions of the sandpaper theory (Radko, 2022a, 2022b, 2023a, 2023b, 2024b). In addition to the arguments based on multiscale asymptotics, the non-monotonic drag pattern has been confirmed by diagnostics of roughness-resolving simulations (Radko, 2023a).

The algorithm used to bridge the fast-flow and slow-flow solutions follows the one adopted in Radko (2024b). The forcing functions are first written as

$$\boldsymbol{D}_i^{(\mathrm{slow})} = -\delta_{n\ i} G^{(\mathrm{slow})} |\overline{\boldsymbol{v}}_i|\, \boldsymbol{s}_i, \quad \boldsymbol{D}_i^{(\mathrm{fast})} = -G_i^{(\mathrm{fast})} |\overline{\boldsymbol{v}}_i|^{-1}\, \boldsymbol{s}_i, \tag{59}$$

where

$$G_i^{(\mathrm{fast})} = 2\pi f^2 \int b_i^2 \left(\upsilon\kappa + \mu\kappa^3 + \frac{\delta_{n\ i}\gamma}{\overline{h}_i \kappa} \right) |\eta_S|^2 \kappa \, d\kappa. \tag{60}$$

In Equation 59, $\boldsymbol{s}_i \equiv \frac{\overline{\boldsymbol{v}}_i}{|\overline{\boldsymbol{v}}_i|}$ denotes the unit vector aligned with the flow, and the normalized attenuation factors (b_i) in Equation 60 are computed from Equation 57. Next, we introduce the analytical function $\Phi_i(|\overline{\boldsymbol{v}}_i|)$ that converges to $\delta_{n\ i} G^{(\mathrm{slow})} |\overline{\boldsymbol{v}}_i|$ and $G_i^{(\mathrm{fast})} |\overline{\boldsymbol{v}}_i|^{-1}$ in the slow-flow and fast-flow limits, respectively. For the bottom layer, we use

$$\Phi_n = \sqrt{G^{(\mathrm{slow})} G_n^{(\mathrm{fast})}} \exp\left(-\sqrt{1 + \ln^2\left(|\overline{\boldsymbol{v}}_n| V_{C\ n}^{-1}\right)} \right). \tag{61}$$

The critical velocity $V_{C\ n} = \sqrt{\frac{G_n^{(\ \mathrm{fast})}}{G^{(\mathrm{slow})}}}$ in Equation 61 represents the transition point between fast-flow and slow-flow regimes. For upper layers $(i = 1, \ldots, n - 1)$, we consider

$$A_i = \tanh^4\left(|\overline{\boldsymbol{v}}_i| V_{C\,b}^{-1}\right) G_i^{(\mathrm{fast})} |\overline{\boldsymbol{v}}_i|^{-1}, \tag{62}$$

where $V_{C\,b} = \sqrt{\frac{G_b^{(\mathrm{fast})}}{G^{(\mathrm{slow})}}}$ and $G_b^{(\mathrm{fast})} = 2\pi \frac{f^2}{\overline{h}_n^2} \int \left(\upsilon\kappa + \mu\kappa^3 + \frac{\gamma}{\overline{h}_n \kappa}\right) |\eta_S|^2 \, d\kappa$. Function (Equation 62) converges to $G_i^{(\mathrm{fast})} |\overline{\boldsymbol{v}}_i|^{-1}$ for $|\overline{\boldsymbol{v}}_i| \gg V_{C\,b}$ but becomes vanishingly small, on the order of $O\left(|\overline{\boldsymbol{v}}_i|^3\right)$, for $|\overline{\boldsymbol{v}}_i| \ll V_{C\,b}$. Both properties conform to the anticipated patterns of the roughness-induced drag in the fast-flow (Section 3.1) and slow-flow (Appendix A) limits. The hybrid model of topographic forcing becomes

$$\boldsymbol{D}_i^{(\mathrm{hybrid})} = -\Phi_i \frac{\overline{\boldsymbol{v}}_i}{\overline{V}_i}. \tag{63}$$

The corresponding evolutionary large-scale equations based on the hybrid model are obtained by replacing $\boldsymbol{D}_i^{(\mathrm{fast})}$ in Equation 54 by $\boldsymbol{D}_i^{(\mathrm{hybrid})}$. In dimensional units, the resulting system takes the form

$$\begin{cases} \dfrac{\partial \overline{\boldsymbol{v}}_i^*}{\partial t^*} + \left(\overline{\boldsymbol{v}}_i^* \cdot \nabla\right) \overline{\boldsymbol{v}}_i^* + \left(-f^* \overline{v}_i^*, f^* \overline{u}_i^*\right) = -\dfrac{1}{\rho_0^*} \nabla \overline{p}_i^* + \upsilon^* \nabla^2 \overline{\boldsymbol{v}}_i^* - \mu^* \nabla^4 \overline{\boldsymbol{v}}_i^* - \delta_{n\ i} \gamma^* \dfrac{\overline{\boldsymbol{v}}_i^*}{h_i^*} + \delta_{1\ i} \dfrac{\boldsymbol{\tau}^*}{\rho_0^* h_i^*} + \boldsymbol{D}_i^{*(\mathrm{hybrid})} \\ \dfrac{\partial \overline{h}_i^*}{\partial t^*} + \nabla \cdot \left(\overline{\boldsymbol{v}}_i^* \overline{h}_i^*\right) = 0, \end{cases} \tag{64}$$

where $\boldsymbol{D}_i^{*(\mathrm{hybrid})} = L^* f_0^{*2} \boldsymbol{D}_i^{(\mathrm{hybrid})}$. This hybrid formulation is well-behaved across all flow speeds. It should be emphasized that the sandpaper theory makes no assumptions regarding the large-scale flow pattern or the boundary conditions. Thus, the roughness-induced drag $D_i^{(\mathrm{hybrid})}$ can be readily incorporated in the momentum equations of any isopycnal model, including comprehensive general circulation models.

4. Implementation and Testing

4.1. Experimental Configuration

To assess the sandpaper model's performance, we consider simulations conducted with HYCOM. The roughness-resolving experiments are compared with solutions based on the parameterized system. To streamline interpretation, the entire analysis is conducted in dimensional units. The asterisks, which previously denoted dimensional quantities, will not be used hereafter. The following system is designed to represent the dynamics of the abyssal ocean, directly affected by seafloor roughness. The reference ocean depth is set to $H_0 = 10^3$ m, and the reduced gravity is assigned a value of $g' \equiv g \frac{\rho_n - \rho_1}{\rho_0} = 10^{-3} \mathrm{m\ s}^{-2}$, which is representative of deep ocean regions. We also assume that the density differences between adjacent layers are identical: $\rho_{i+1} - \rho_i = \frac{\rho_n - \rho_1}{n-1}$. The calculations are performed on the f-plane with $f = 10^{-4}\ \mathrm{s}^{-1}$, and the dissipation parameters are $\upsilon = 10\ \mathrm{m}^2\ \mathrm{s}^{-1}$ and $\mu = \gamma = 0$. The chosen υ is consistent with values used in comprehensive roughness-resolving HYCOM simulations (e.g., Chassignet & Xu, 2021; Chassignet et al., 2023). We configure HYCOM with 10 layers of background thickness of 100 m each.

The non-local model is tested on the canonical vortex spin-down problem. We consider an initially barotropic Gaussian vortex

$$\psi = C \exp\left(-\frac{r^2}{R^2}\right), \quad r = \sqrt{x^2 + y^2}, \tag{65}$$

where ψ is the streamfunction associated with the velocity field $(u_i, v_i) = \left(-\frac{\partial \psi}{\partial y}, \frac{\partial \psi}{\partial x}\right)$, and $R = 5 \times 10^4$m is an effective radius. The amplitude $C = 5 \times 10^3 \mathrm{m}^2 \mathrm{s}^{-1}$ used in simulations corresponds to the maximal radial velocity of $V_{\max} = 0.086\ \mathrm{m\ s}^{-1}$. We assume doubly periodic lateral boundary conditions and employ a relatively wide computational domain of size $(L_x, L_y) = \left(4 \cdot 10^5 \mathrm{m}, 4 \cdot 10^5 \mathrm{m}\right)$, which minimizes the influence of boundaries on the vortex dynamics.

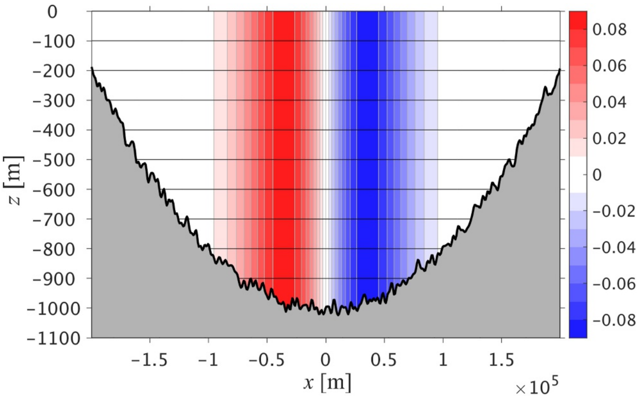

Figure 2. The zonal section across the center of the computational domain used in the roughness-resolving BOWL experiments. The horizontal lines indicate the density interfaces, which often intersect bathymetry. The red-blue pattern represents the initial meridional velocity $v_i\left[\mathrm{m\ s^{-1}}\right]$ associated with the Gaussian streamfunction (Equation 65).

Topography is represented by irregular small-scale variability based on the observationally derived spectrum of Goff and Jordan (1988):

$$P_{GJ} = \frac{\mu-2}{(2\pi)^3}\left(\frac{\eta_{GJ}}{k_0 l_0}\right)^2\left(1+\left(\frac{k}{2\pi k_0}\right)^2+\left(\frac{l}{2\pi l_0}\right)^2\right)^{-7/4}, \tag{66}$$

where η_{GJ} is an adjustable coefficient that allows us to specify the desired roughness magnitude. The original spectrum was substantially anisotropic, as reflected by unequal effective wavenumbers—zonal $\left(k_0 = 2.3 \times 10^{-4}\mathrm{m}^{-1}\right)$ and meridional $\left(l_0 = 1.3 \times 10^{-4}\mathrm{m}^{-1}\right)$. However, to unambiguously assess the performance of the sandpaper model, which in its present form assumes isotropic roughness, we follow Nikurashin et al. (2014) and consider

$$k_0 = l_0 = 1.8 \times 10^{-4}\mathrm{m}^{-1}. \tag{67}$$

The small-scale topography in physical space (η_S) is obtained as a sum of Fourier modes with random phases and spectral amplitudes conforming to Equation 66. The wavelengths of these modes are constrained from above and below:

$$L_{\min} < \frac{2\pi}{\kappa} < L_{\max}. \tag{68}$$

We assume $L_{\max} = 3 \times 10^4$ m to satisfy Equation 9 and $L_{\min} = 3 \times 10^3$ m to ensure that all topographic scales are well resolved. The spectrum is normalized so that the root-mean-square small-scale depth variation is $\eta_{\mathrm{rms}} = 15$ m. Two sets of simulations are presented. The first set considers flat large-scale bathymetry and will be referred to as FLAT hereafter. The total depth is given by

$$\mathrm{FLAT}: H = H_0 - \eta_S(x,y), \tag{69}$$

which is used to explore isopycnal surfaces that do not intersect with rough topography. Therefore, the FLAT simulations enable us to assess the merits of local and non-local parameterizations. The second set examines circulation in the basin, where depth varies at both large and small scales. It will be denoted as BOWL, reflecting the bowl-shaped domain (Figure 2) used in these simulations. The depth pattern is given by

$$\mathrm{BOWL}: H = H_0 - ar^2 - \eta_S(x,y), \tag{70}$$

where $a = \frac{50}{R^2} = 2 \times 10^{-8}\mathrm{m}^{-1}$, and r is the distance from the domain center. In these experiments, the isopycnals intersect the topography, and layers vanish $\left(\overline{h}_i \to 0\right)$ in some locations, which the local model cannot handle. In all sandpaper simulations, the explicit small-scale variability in bottom topography is removed $\left(\eta_S = 0\right)$ to prevent double-counting of roughness-induced forcing. The analysis of both FLAT and BOWL systems focuses on comparing non-local parametric and roughness-resolving simulations.

4.2. FLAT Simulations

Our first example is the roughness-resolving FLAT simulation performed on a fine mesh with $(N_x, N_y) = (512, 512)$ grid points. Figure 3 presents the absolute values of total velocity $|\boldsymbol{v}_i|$ and its small-scale component $|\boldsymbol{v}_{S\,i}|$ in layers $i = 8$, 9, and 10 realized at $t = 10$ days in the roughness-resolving FLAT simulation. The small-scale velocity $(u_{S\,i}, v_{S\,i})$ was obtained by removing Fourier components of (u_i, v_i) with wavelengths exceeding $L_{\max}$.

The velocity patterns in Figure 3 reflect the presence of small-scale eddies in deep layers. Their intensity, however, rapidly decreases away from the seafloor. These results are consistent with the proposed scaling for the vertical extent of a region directly affected by roughness (Radko, 2022b):

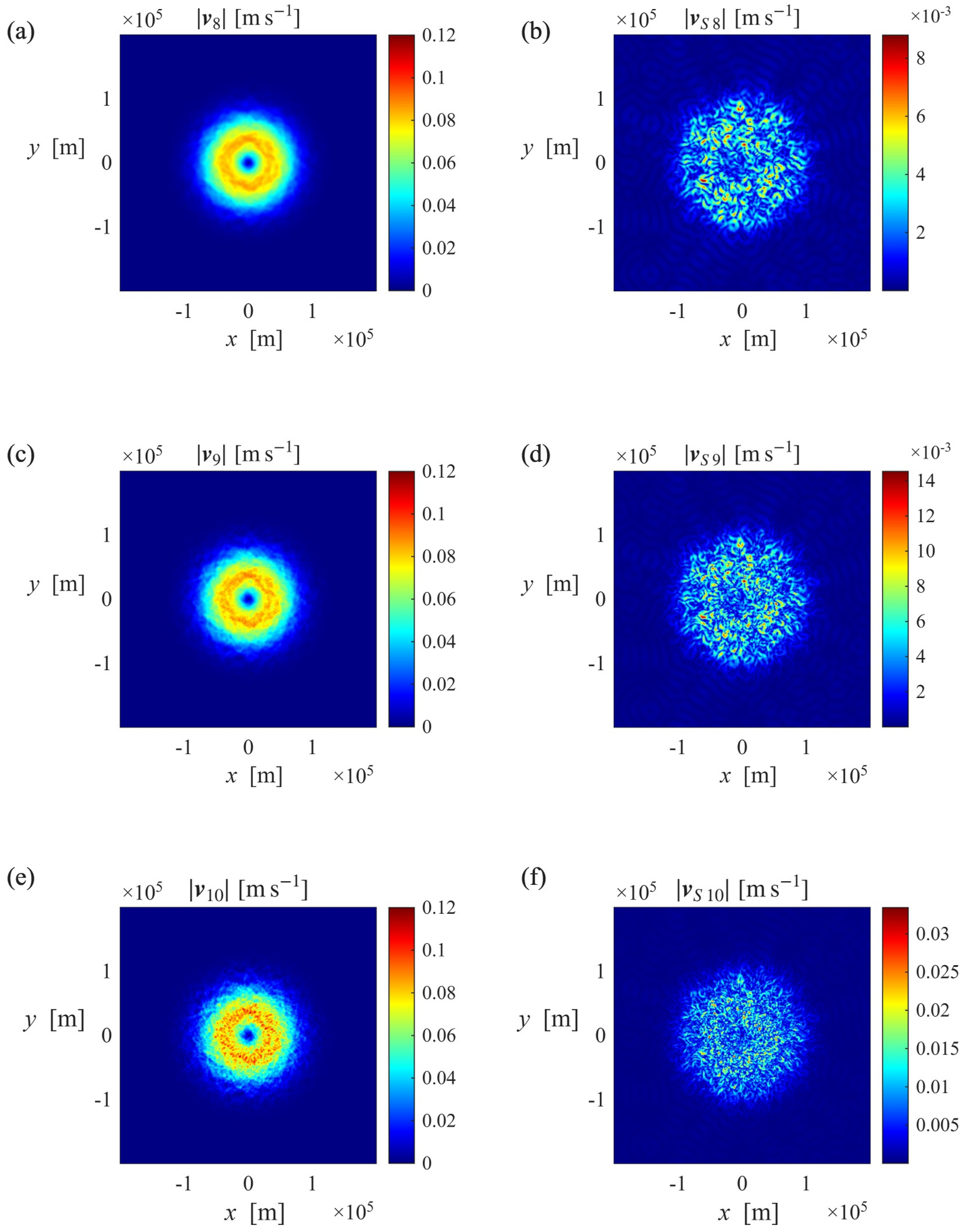

Figure 3. The roughness-resolving HYCOM simulation in the FLAT category. The instantaneous patterns of the absolute velocities (left panels) and their small-scale components (right panels) are shown for $t = 10$ days. Panels (a, b), (c, d), and (e, f) represent layers 8, 9, and 10, respectively.

$$h_{\text{eff}} \sim \frac{f}{N\kappa_S}, \tag{71}$$

where $N \sim \sqrt{\frac{g'}{H_0}}$ is the buoyancy frequency and κ_S is the representative wavenumber of small-scale topography. Scaling (Equation 71) also matches the attenuation of perturbations in continuously stratified quasi-geostrophic

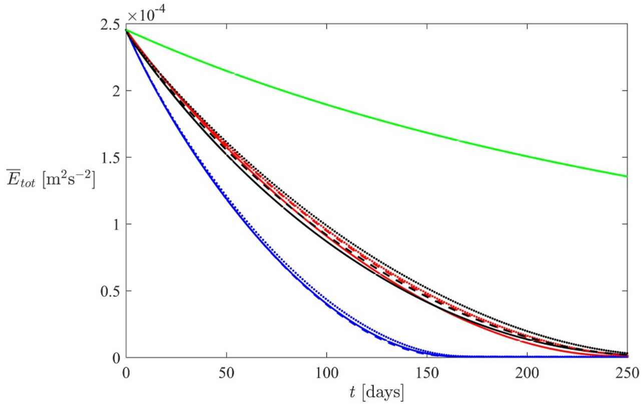

Figure 4. The time series of the mean domain-integrated large-scale kinetic energy $\overline{E}_{\text{tot}}$ for simulations in the FLAT category. The roughness-resolving, non-local parametric, and local parametric simulations are indicated by black, red, and blue curves, respectively. Solid curves represent HYCOM-based simulations. Also included are the results of the quasi-geostrophic (dotted curves) and shallow-water (dashed curves) spectral simulations. The overlapping green curves represent smooth topography $(\eta_S = 0)$ simulations.

models (e.g., Vallis, 2019). For the present configuration, $h_{\text{eff}} \sim 100$ m, which explains the patterns observed in Figure 3. In the upper layers ($i = 1, 2, \ldots, 7$), the small-scale signal is weak and largely inconsequential.

To examine the temporal pattern of the vortex spin-down, Figure 4 presents the time series of the net volume-averaged large-scale kinetic energy $\overline{E}_{\text{tot}}(t) = \frac{1}{2}\langle \overline{u}^2 + \overline{v}^2 \rangle_{x,y,z}$. In each layer, the large-scale velocity components $(\overline{u}_i, \overline{v}_i)$ are computed by retaining harmonics of (u_i, v_i) with wavelengths exceeding $L_{\max}$. These are the flow components that the sandpaper theory is designed to represent. The kinetic energy in the roughness-resolving HYCOM simulation, indicated by the solid black curve in Figure 4, monotonically decreases in time, and the spin-down is effectively completed by $t = 250$ days. The analogous parametric simulation is performed using the non-local sandpaper model (Equation 64), in which the attenuation factors are computed using (Equation 57). As will be seen shortly, parametric simulations are largely insensitive to resolution, and those in Figure 4 are based on $(N_x, N_y) = (256, 256)$.

$\overline{E}_{\text{tot}}(t)$ in the parametric model (solid red curve in Figure 4) closely follows the roughness-resolving calculation. The non-local sandpaper theory underestimates the vortex energy throughout the entire simulation, but the differences are small ($\Delta E < 1.7 \times 10^{-8}\text{m}^2\text{s}^{-2}$). We also note that the computational overhead of parametric simulations associated with evaluating the roughness-induced drag components could be effectively eliminated by increasing the periodicity $(\Delta t_{\text{update}})$ of updates of the attenuation coefficients b_i. For moderate Δt_{update}, this approach does not lead to the substantial loss of accuracy. For instance, the relative difference in $\overline{E}_{\text{tot}}$ for simulations in which attenuation coefficients were updated at each step $(\Delta t_{\text{update}} = 5\text{ s})$ and once every hour $(\Delta t_{\text{update}} = 3600\text{ s})$ is typically on the order of 10^{-6}.

To quantify the relative benefits of local and non-local formulations, we present (Figure 4) the simulation performed using the local sandpaper model (solid blue curve). The numerical algorithm is modified by assigning the attenuation factors $a_i = \delta_{n\ i}$—values that define the local formulation. Figure 4 indicates that the local model substantially overestimates the vortex decay rate. Its poor performance in the current configuration is unsurprising. The local model assumes from the outset that the roughness-induced perturbations are wholly contained in the bottom layer, which demands that $h_{\text{eff}} \ll h_n$. However, at present, we use a relatively fine vertical discretization with $h_{\text{eff}} \sim h_n$, violating the very assumption of the perturbation locality.

To ensure that the results in Figure 4 are not model-dependent, we have reproduced the FLAT HYCOM simulations using the Fourier-based spectral dealiased model employed in our previous studies. Two versions of the spectral model have been considered. The first model (dashed curves in Figure 4) integrates the shallow-water equations and their parametric counterparts (Radko, 2024b). The second spectral model (Radko, 2023a) is based on the quasi-geostrophic framework (e.g., Pedlosky, 1987, Chapter 6) and is indicated by dotted curves. Since the algorithms in all models differ substantially, their close agreement lends further credence to our findings. Another interesting feature of Figure 4 is the consistency of shallow-water and quasi-geostrophic simulations. In the quasi-geostrophic model, finite-amplitude thickness variation and ageostrophic velocities are treated as higher-order corrections. However, the assumption of weak variation in layer thickness is at odds with the distribution of h_{10}, which varies by up to 60% relative to the global mean. Thus, the agreement of quasi-geostrophic and shallow-water models implies that processes not captured by the quasi-geostrophic model have a limited impact on roughness-induced bottom drag. We find this result particularly encouraging, given the substantial conceptual insights and computational gains afforded by quasi-geostrophic approximation.

Overall, the diagnostics in Figure 4 reinforce our belief that seafloor roughness can substantially impact the evolution of large-scale oceanic flows (LaCasse et al., 2019; Radko, 2023a, 2023b). This point is illustrated by presenting the smooth-bottom $(\eta_S = 0)$ simulation. The vortex evolution in this experiment is qualitatively dissimilar to its rough-bottom counterpart, and the decay rates differ by a factor of three. It should also be noted that the roughness level considered in this study is relatively low $(\eta_{\text{rms}} = 15\text{ m})$. The small-scale variability in

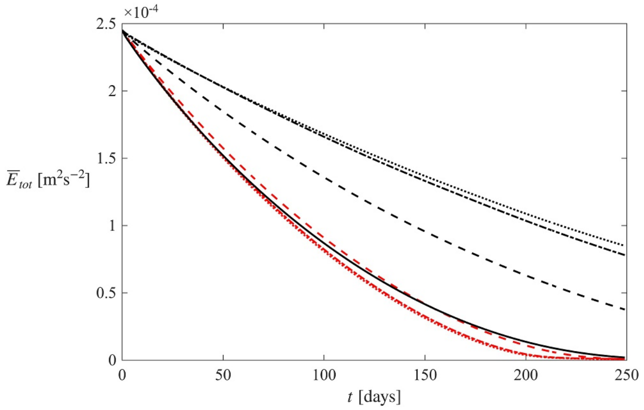

Figure 5. The impact of resolution on the accuracy of the explicit-topography (black curves) and parametric (red curves) simulations. Time series of the domain-averaged large-scale kinetic energy $\overline{E}_{\rm tot}$ in FLAT simulations are shown for $N_x \times N_y = 512 \times 512$ (solid curves), 256×256 (dashed curves), 128×128 (dot-dashed curves), and 64×64 (dotted curves).

many regions of the World Ocean is much more pronounced, with $\eta_{\rm rms} > 300$ m not uncommon (Goff, 2020). Yet, even the present, relatively mild roughness dramatically accelerates spin-down.

Figure 5 examines how the performance of parametric and explicit-topography HYCOM simulations is affected by changes in resolution. The design of all experiments in Figure 5 matches the baseline simulation (Figure 3), but the lateral mesh ($N_x \times N_y$) is systematically coarsened. In the explicit-topography simulations, we use the depth data from the fully resolved experiment (Figure 4) at every other grid point for $N_x \times N_y = 256 \times 256$, every fourth for 128×128, and every eighth for 64×64 cases. As expected, the coarsening of the explicit-topography experiments leads to a dramatic loss of accuracy. In contrast, parametric simulations proved to be largely insensitive to changes in resolution.

4.3. BOWL Simulations

One of the motivating factors for developing the non-local theory was the requirement that the parametric model perform well even near intersections of isopycnals with topography. Since the depth of the bottom layer at such locations approaches zero, the local parametrization is inapplicable there. The question arises as to how accurate the non-local parametrization might be under such challenging conditions. To that end, we use the computational domain shown in Figure 2, in which density interfaces intersect the bathymetry at several locations. The spectral models (Section 4.2) are not designed to treat such systems, and therefore, we present only HYCOM-based simulations.

Aside from differences in bathymetry, the design of BOWL simulations follows that of their FLAT counterparts. The temporal record of the total energy is shown in Figure 6. As expected, the attempt to use the local parameterization has resulted in a catastrophic failure of the simulation. Therefore, Figure 6 presents the roughness-resolving simulation (black curve) and the non-local parameterization (red). The parametric and roughness-resolving $\overline{E}_{\rm tot}(t)$ patterns are generally consistent, although the sandpaper theory tends to overestimate the energy.

While the diagnostics in Figure 6 focused on the system's integral properties, we also find it instructive to examine the evolutionary patterns of individual layers. Particularly interesting are the dynamics of the tenth layer. It is located immediately above rough topography, and its thickness gradually reduces from the maximal value at the vortex center to zero at $r \approx 7 \times 10^4$m. These features make the tenth layer particularly vulnerable to the roughness-induced forcing. Therefore, we present (Figure 7) the time series of the mean large-scale kinetic energy in the tenth layer ($\overline{E}_{10}$). Figure 7 suggests that the roughness-resolving and non-local parametric patterns of $\overline{E}_{10}(t)$ are generally consistent, although the sandpaper theory tends to underestimate the vortex spin-down rate. As in the FLAT configuration, the parametric simulations in Figures 6 and 7 are largely insensitive to resolution. On the other hand, the coarse-grid and fully resolved explicit topography experiments yield inconsistent estimates.

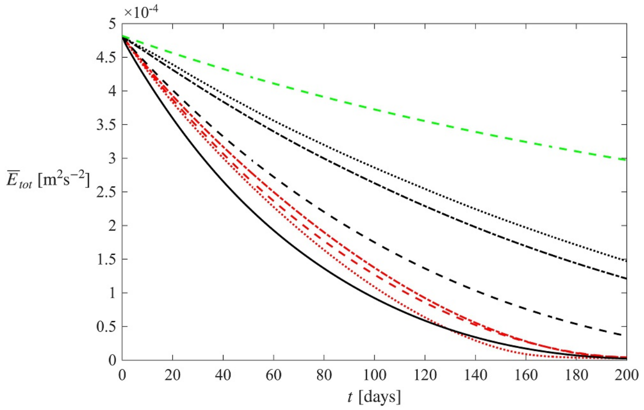

Figure 6. The time series of the domain-averaged large-scale kinetic energy $\overline{E}_{\rm tot}$ in the BOWL simulations. The explicit-topography and non-local parametric simulations are indicated by black and red curves, respectively. The green curve represents the smooth topography $(\eta_S = 0)$ simulation. Simulations performed with $N_x \times N_y = 512 \times 512, 256 \times 256, 128 \times 128$, and 64×64 are indicated by solid, dashed, dot-dashed, and dotted curves, respectively.

5. Discussion

The rough topography of the ocean basins presents a major challenge for theoretical analyses of circulation, numerical modeling, and the interpretation of field measurements. The cumulative impact of kilometer-scale topographic features on much broader flow patterns can be dramatic (LaCasce et al., 2019; Radko, 2020) and, in some cases, lead to unexpected consequences (e.g., Gulliver & Radko, 2022). Yet, these small-scale seafloor patterns are unresolved by global climate and operational predictive systems, and our ability to concisely represent roughness effects remains limited. Empirical drag laws currently used by general circulation models do not capture the dynamics of roughness-induced forcing, motivating efforts to design more targeted closure schemes.

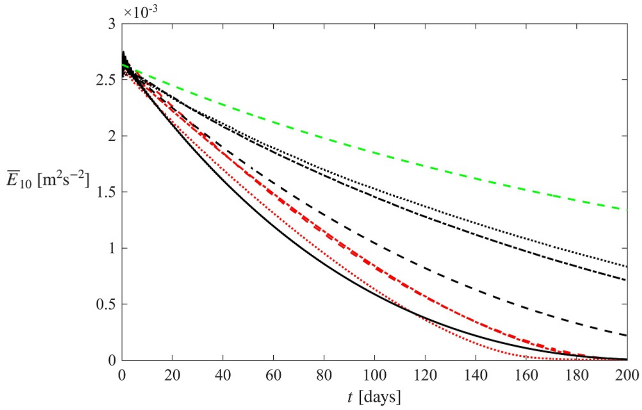

Figure 7. The same as in Figure 6, but for the mean large-scale kinetic energy in the tenth layer ($\overline{E}_{10}$).

Our previous attempts to develop physics-based parameterizations of roughness have led to the so-called sandpaper model (Radko, 2024a, 2024b). This model is based on the multiscale asymptotic analysis of governing equations. Therefore, unlike many other closures, it does not rely on empirical assumptions. As a result, the sandpaper theory is dynamically transparent, and the mechanisms of flow-roughness interaction can be unambiguously interpreted by considering balances arising at each order in the expansion. For instance, the key property of the model's fast-flow limit is the homogenization of small-scale PV in the abyssal layer, which results in the counterintuitive reduction of the roughness-induced drag with increasing velocity. Another appealing feature of the sandpaper model is that it circumvents the need to consider specific patterns of small-scale topography, which vary by location. Instead, it focuses on the statistical spectrum of bathymetry, which holds promise of a more universal description of roughness-induced forcing. The sandpaper theory has been tested by modeling various baroclinic and barotropic phenomena, including the spinning-down vortex (Radko, 2022a, 2022b), forced large-scale flows interacting with multiscale topography (Radko, 2023b, 2024b), and free Rossby waves (Davis et al., 2025). In all cases, the evolutionary large-scale patterns predicted by the sandpaper theory matched those from the corresponding roughness-resolving simulations.

The key shortcoming of these early efforts is the assumption of locality. The lowest isopycnal layer was assumed to be deep enough to encompass the entire region of the roughness's direct influence. This assumption can be violated when the vertical resolution in the abyssal ocean is systematically increased (see the schematic in Figure 1). Limitations of the local formulation become particularly apparent in the context of operational ocean simulations that use isopycnic coordinates, such as the Navy Global Ocean Forecast System (Metzger et al., 2014), which is currently based on HYCOM. In these realistic configurations, density interfaces frequently intersect bathymetry, and the roughness-induced drag predicted by the local model becomes singular. It unphysically increases without bound, precluding the implementation of the sandpaper closure in its original form. The singularity of roughness-induced drag is shown to be a direct consequence of the locality approximation used in earlier sandpaper models.

To overcome the deficiencies of the local closure, we develop a non-local sandpaper model that accounts for small-scale variability in layers not in direct contact with the seafloor. The physical processes captured by the new theory are dynamically analogous to the previously identified forcing mechanisms in the local model. However, unlike its local antecedent, the interaction of primary flows with rough terrain in the non-local model introduces small-scale variability throughout the water column. These topographically induced eddies, in turn, affect large-scale circulation patterns through the eddy form drag and Reynolds stresses. The non-local formulation is implemented in HYCOM, a mainstream general circulation model, thereby facilitating the adoption of sandpaper closure by the modeling community. The theory-based parameterization is tested on the canonical vortex spin-down problem and shown to be consistently more accurate than its local counterpart.

While our preliminary results are encouraging, testing and validation of the non-local model should be extended to progressively more complex and realistic configurations. The wind-driven double-gyre system with corrugated bathymetry represents a natural advancement, permitting concurrent assessment of the sandpaper model in swift boundary currents and broad interior flows. A separate question concerns the geographic variability of ocean roughness. While the sandpaper theory permits large-scale modulation of small-scale topography, current validation efforts (Section 4) have been limited to systems with uniform roughness. Yet another aspect that requires systematic analysis is the performance of the sandpaper closure in eddy-resolving, eddy-permitting, and non-eddying circulation models. Beyond the pragmatic interest in improving the fidelity of numerical forecasts, the non-local model may also yield further theoretical advancements. Of particular interest is the extension of the sandpaper formalism to continuously stratified systems. One pathway to the development of a fully three-dimensional z-coordinate sandpaper model is the analysis of the asymptotic thin-layer limit $\Delta\rho = \max\limits_{1\le i\le n-1}\{\rho_{i+1} - \rho_i\} \to 0$. This regime would have been inaccessible through its local formulation, which a priori assumes a sufficiently deep bottom layer. However, the non-local theory effectively removes the restriction on vertical discretization, making the model more flexible and general.

Another theoretical development should target non-isotropic bathymetric spectra. The observationally derived spectrum of Goff and Jordan (1988) accounts for the anisotropy of the seafloor by introducing two distinct effective wavenumbers in Equation 66, zonal (k_0) and meridional (l_0). For simplicity, the present parameterization assumes an isotropic model based on the average wavenumber. It remains to be determined whether this approximation introduces substantial bias. If it does, the sandpaper formulation should be generalized to account for the unequal values of k_0 and l_0. A separate line of investigation should address the contribution of flow-blocking and lee waves to roughness-induced drag (e.g., Klymak et al., 2021). In the present formulation of the asymptotic model, the leading-order component of roughness-induced forcing is controlled by dissipative processes. The aspect is consistent with simulations (Section 4), which show excellent agreement between parametric and more general roughness-resolving experiments. However, this property should not be taken for granted, particularly for more realistic and complex systems. It may prove prudent to extend the asymptotic expansion to include non-dissipative higher-order components of roughness-induced forcing. There are numerous other enhancements and extensions of the sandpaper model on our wish list. They include, but are not limited to, non-hydrostatic effects, roughness-induced water mass transformation, interaction of small-scale topography with tides, and more precise interactive models of explicit dissipation. Nevertheless, we believe that our general approach, which is based on the statistical roughness spectrum rather than on specific spatial patterns, will remain highly beneficial in future flow-topography interaction studies.

Appendix A: The Slow-Flow Model

To identify the essential dynamics of flow-topography interaction of low Reynolds number flows, we consider the asymptotic sector $U = O(\varepsilon^2)$ and $\upsilon = O(\varepsilon)$, which corresponds to $\mathrm{Re} = \frac{L^* U^*}{\upsilon^*} = O(\varepsilon)$. The solutions obtained in this sector will be referred to as the slow-flow model. The temporal variability in this low-Re regime is expected to be controlled by dissipative processes rather than by mean-field advection. The dissipative processes in the slow-flow model operate on the timescale $T_3 = \varepsilon^3 t$, and therefore, temporal derivatives in governing equations are replaced by $\frac{\partial}{\partial t} \to \varepsilon^3 \frac{\partial}{\partial T_3}$. The frictional parameters and small-scale bathymetric variability are rescaled as follows:

$$\upsilon = \varepsilon \upsilon_0, \quad \mu = \varepsilon \mu_0, \quad \gamma = \varepsilon \gamma_0, \quad \eta_S = \varepsilon^2 \eta_{S0}. \tag{A1}$$

We seek the solution in terms of the following power series for velocity

$$\boldsymbol{v}_i = \varepsilon^2 \boldsymbol{v}_i^{(2)}(X, Y, T_3) + \sum_{j=3}^{\infty} \varepsilon^j \boldsymbol{v}_i^{(j)}(X, Y, x, y, T_3), \tag{A2}$$

and pressure

$$p_i = p_i^{(0)}(X, Y, T_3) + \varepsilon p_i^{(1)}(X, Y, T_3) + \varepsilon^2 p_i^{(2)}(X, Y, T_3) + \sum_{j=3}^{\infty} \varepsilon^j p_i^{(j)}(X, Y, x, y, T_3). \tag{A3}$$

The layer thicknesses are still represented by Equation 23.

Following the approach used in Section 3, we first compute the leading-order perturbation balances. For the momentum equations, it is realized at $O(\varepsilon^3)$:

$$\begin{cases} f {v'}_i^{(3)} = \dfrac{\partial {p'}_i^{(3)}}{\partial x} \\ f {u'}_i^{(3)} = -\dfrac{\partial {p'}_i^{(3)}}{\partial y}. \end{cases} \tag{A4}$$

The key insights into the dynamics are brought by the small-scale $O(\varepsilon^4)$ balance of the PV equation (Equation 7):

$$u_i^{(2)}\frac{\partial q'^{(2)}}{\partial x} + v_i^{(2)}\frac{\partial q'^{(2)}}{\partial y} = \frac{\upsilon_0}{h_i^{(0)}}\nabla^2\varsigma'^{(2)}_i - \frac{\mu_0}{h_i^{(0)}}\nabla^4\varsigma'^{(2)}_i - \frac{\delta_{n\ i}\gamma_0}{h_i^{(0)2}}\varsigma'^{(2)}_i, \tag{A5}$$

where

$$q'^{(2)}_i = -\frac{f h'^{(2)}_i}{\left(h_i^{(0)}\right)^2}. \tag{A6}$$

The leading order small-scale component of the recursive relation (Equation 6) takes the form

$$B_{i,i+1}\sum_{j=1}^{i} h'^{(2)}_j = 0, \quad i = 1,\ldots,n-1, \tag{A7}$$

and when it is combined with Equation 35, we conclude that

$$h'^{(2)}_i = -\delta_{n\ i}\eta_{S0}. \tag{A8}$$

This result underscores the fundamental difference between the effects of roughness in fast and slow flows. While the vertical attenuation factor (a_i) in the fast-flow model attained finite values in several layers, the reduction in the flow speed for the same stratification pattern $(B_{i,i+1})$ has led to the localization of a roughness signal to the lowest layer: $a_i = \delta_{n\ i}$. In retrospect, this conclusion appears natural and physical since the flow speed undoubtedly controls the vertical transmission of the roughness signal. In the limiting case of a quiescent system, one expects density interfaces to flatten. In this regime, Equations A4–A6 can be solved for small-scale velocity components as functions of roughness. The calculation is performed in the Fourier space and results in:

$$\begin{cases} \tilde{u}'^{(3)}_n = \dfrac{fl\left(ku_n^{(2)} + lv_n^{(2)}\right)}{\left(h_n^{(0)}\upsilon_0\kappa^2 + h_n^{(0)}\mu_0\kappa^4 + \gamma_0\right)\kappa^2}\tilde{\eta}_{S0} \\ \tilde{v}'^{(3)}_n = -\dfrac{fk\left(ku_n^{(2)} + lv_n^{(2)}\right)}{\left(h_n^{(0)}\upsilon_0\kappa^2 + h_n^{(0)}\mu_0\kappa^4 + \gamma_0\right)\kappa^2}\tilde{\eta}_{S0.} \end{cases} \tag{A9}$$

and $\widetilde{\boldsymbol{v}'}^{(3)}_i = 0$ for $i < n$.

The evolutionary large-scale system is obtained using the $O(\varepsilon^5)$ mean momentum equations:

$$\frac{\partial \boldsymbol{v}_i^{(2)}}{\partial T_3} + \left(-f\left\langle v_i^{(5)}\right\rangle, f\left\langle u_i^{(5)}\right\rangle\right) = -\nabla_X\left\langle p_i^{(3)}\right\rangle - \delta_{n\ i}\gamma_0\frac{\left\langle \boldsymbol{v}_n^{(4)}\right\rangle}{h_n^{(0)}}, \tag{A10}$$

and $O(\varepsilon^7)$ thickness equation:

$$\frac{\partial\left\langle h_i^{(4)}\right\rangle}{\partial T_3} + \frac{\partial}{\partial X}\left(\sum_{j=2}^{5}\left\langle u_i^{(j)}\right\rangle\left\langle h_i^{(5-j)}\right\rangle + \left\langle u'^{(3)}_i h'^{(2)}_i\right\rangle\right) + \frac{\partial}{\partial Y}\left(\sum_{j=2}^{5}\left\langle v_i^{(j)}\right\rangle\left\langle h_i^{(5-j)}\right\rangle + \left\langle v'^{(3)}_i h'^{(2)}_i\right\rangle\right) = 0. \tag{A11}$$

The large-scale forcing by the small-scale eddies is now represented by terms $\left\langle u'^{(3)}_i h'^{(2)}_i\right\rangle$ and $\left\langle v'^{(3)}_i h'^{(2)}_i\right\rangle$ in the thickness equation (Equation A11). It is interesting that, while Reynolds stresses played a significant role in the fast-flow model, they are now conspicuously absent from the momentum equations. Importantly, the roughness-induced forcing at this order is active only in the bottom layer $(i = n)$.

Following the approach adopted for the fast-flow model, we incorporate the eddy transfer of thickness components into the residual-mean velocities (Andrews & Mcintyre, 1976):

$$\boldsymbol{v}_{res\ i} = \left\langle \boldsymbol{v}_i^{(5)} \right\rangle + \frac{\left\langle \boldsymbol{v}'^{(3)}_i h'^{(2)}_i \right\rangle}{h_i^{(0)}}. \tag{A12}$$

The eddy transfer terms are linked to the large-scale flow properties by combining Equation A8 with Equation A9 and applying the Parseval identity (Equation 15):

$$\begin{cases} \left\langle u'^{(3)}_n h'^{(2)}_n \right\rangle = -\pi v_n^{(2)} f \displaystyle\int \frac{\left|\tilde{\eta}_{S0}\right|^2 \kappa}{h_n^{(0)} \upsilon_0 \kappa^2 + h_n^{(0)} \mu_0 \kappa^4 + \gamma_0} d\kappa \\ \left\langle v'^{(3)}_n h'^{(2)}_n \right\rangle = \pi u_n^{(2)} f \displaystyle\int \frac{\left|\tilde{\eta}_{S0}\right|^2 \kappa}{h_n^{(0)} \upsilon_0 \kappa^2 + h_n^{(0)} \mu_0 \kappa^4 + \gamma_0} d\kappa. \end{cases} \tag{A13}$$

Finally, we obtain the evolutionary large-scale equations by (i) introducing the following large-scale field variables:

$$\overline{\boldsymbol{v}}_i = \sum_{j=2}^{4} \varepsilon^j \left\langle \boldsymbol{v}_i^{(j)} \right\rangle + \varepsilon^5 \boldsymbol{v}_{res\ i}, \quad \overline{h}_i = \sum_{j=0}^{4} \varepsilon^j \left\langle h_i^{(j)} \right\rangle, \quad \overline{p}_i = \sum_{j=1}^{3} \varepsilon^j \left\langle p_i^{(j)} \right\rangle, \tag{A14}$$

(ii) combining all (x,y)-averaged balances, and (iii) reverting to the original independent variables (x,y,t). The resulting system takes the form

$$\begin{cases} \dfrac{\partial \overline{\boldsymbol{v}}_i}{\partial t} + \left(-f\overline{v}_i, f\overline{u}_i\right) = -\nabla \overline{p}_i - \delta_{n\ i} \gamma \dfrac{\overline{\boldsymbol{v}}_i}{h_i} + \delta_{1\ i} \dfrac{\boldsymbol{\tau}}{h_i} + \delta_{n\ i} \boldsymbol{D}_n^{(\mathrm{slow})} \\ \dfrac{\partial \overline{h}_i}{\partial t} + \nabla \cdot \left(\overline{\boldsymbol{v}}_i \overline{h}_i\right) = 0\,. \end{cases} \tag{A15}$$

The roughness-induced forcing $\boldsymbol{D}_n^{(\mathrm{slow})}$ in Equation A15 can be expressed as

$$\boldsymbol{D}_n^{(\mathrm{slow})} = -G^{(\mathrm{slow})} \overline{\boldsymbol{v}}_n, \tag{A16}$$

where

$$G^{(\mathrm{slow})} = \frac{\pi f^2}{\overline{h}_n} \int \frac{\left|\tilde{\eta}_S\right|^2 \kappa}{\overline{h}_n \upsilon \kappa^2 + \overline{h}_n \mu \kappa^4 + \gamma} d\kappa. \tag{A17}$$

The forcing term Equation A16 represents the so-called form drag, which is caused by the pressure differences between the upstream and downstream sides of topographic features:

$$\boldsymbol{D}_n^{(\mathrm{slow})} \approx \frac{1}{\overline{h}_n} \left\langle \nabla \overline{p}_n\, \eta_S \right\rangle = -\frac{1}{\overline{h}_n} \left\langle \overline{p}_n \nabla \eta_S \right\rangle. \tag{A18}$$

This forcing mechanism is dissimilar to the one that controls the evolution of fast flows (Section 3.1)—the latter also relies on Reynolds stresses associated with roughness-generated eddies. For implementation in comprehensive models, it may be prudent to introduce the following correction to the slow-flow model (Equation A17):

$$\overline{h}_n \rightarrow \overline{h}_n + \mathrm{rms}(\eta_S), \tag{A19}$$

which precludes the model's singularity at locations where concurrently $\overline{h}_n \to 0$ and $|\overline{\mathbf{v}}_n| \to 0$. Since the theoretical model from the outset assumes $(\overline{h}_n, \eta_S) \sim (1, \varepsilon^2)$, approximation (Equation A19) does not affect the asymptotic accuracy of the solution.

Conflict of Interest

The authors declare no conflicts of interest relevant to this study.

Availability Statement

Data sets produced in this study are available in Radko (2026), located at https://doi.org/10.6084/m9.figshare.30141550. The relevant HYCOM subroutines are included in the file HYCOM_NLsandpaper.tar.

Acknowledgments

Support of the National Science Foundation (Grants OCE 2241625 and 2241626) and the Office of Naval Research (Grant O2502017017085061) is gratefully acknowledged. The authors thank the JAMES editors (Dr. Griffies and Grooms) and the anonymous reviewers for helpful comments.

References

Andrews, D. G., & Mcintyre, M. E. (1976). Planetary waves in horizontal and vertical shear: The generalized Eliassen-Palm relation and the mean zonal acceleration. *Journal of the Atmospheric Sciences*, *33*(11), 2031–2048. https://doi.org/10.1175/1520-0469(1976)033<2031:pwihav>2.0.co;2

Bleck, R. (2002). An oceanic general circulation model framed in hybrid isopycnic-Cartesian coordinates. *Ocean Modelling*, *4*(1), 55–88. https://doi.org/10.1016/s1463-5003(01)00012-9

Chassignet, E. P., Hurlburt, H. E., Metzger, E. J., Smedstad, O. M., Cummings, J., Halliwell, G. R., et al. (2009). U.S. GODAE: Global Ocean Prediction with the HYbrid Coordinate Ocean Model (HYCOM). *Oceanography*, *22*(2), 64–75. https://doi.org/10.5670/oceanog.2009.39

Chassignet, E. P., Hurlburt, H. E., Smedstad, O. M., Halliwell, G. R., Wallcraft, A. J., Metzger, E. J., et al. (2006). Generalized vertical coordinates for eddy-resolving global and coastal ocean forecasts. *Oceanography*, *19*(1), 20–31. https://doi.org/10.5670/oceanog.2006.95

Chassignet, E. P., Smith, L. T., Halliwell, G. R., & Bleck, R. (2003). North Atlantic simulations with the HYbrid Coordinate Ocean Model (HYCOM): Impact of the vertical coordinate choice, reference density, and thermobaricity. *Journal of Physical Oceanography*, *33*(12), 2504–2526. https://doi.org/10.1175/1520-0485(2003)033<2504:naswth>2.0.co;2

Chassignet, E. P., & Xu, X. (2021). On the importance of high-resolution in large-scale ocean models. *Advances in Atmospheric Sciences*, *38*(10), 1621–1634. https://doi.org/10.1007/s00376-021-0385-7

Chassignet, E. P., Xu, X., Bozec, A., & Uchida, T. (2023). Impact of the New England seamount chain on Gulf Stream pathway and variability. *Journal of Physical Oceanography*, *53*(8), 1871–1886. https://doi.org/10.1175/jpo-d-23-0008.1

Davis, T., Radko, T., Brown, J., & Dewar, W. (2025). Rough topography and fast baroclinic Rossby waves. *Geophysical Research Letters*, *52*(2), e2024GL112589. https://doi.org/10.1029/2024gl112589

Dewar, W. K. (1986). On the potential vorticity structure of weakly ventilated isopycnals: A theory of subtropical mode water maintenance. *Journal of Physical Oceanography*, *16*(7), 1204–1216. https://doi.org/10.1175/1520-0485(1986)016<1204:otpvso>2.0.co;2

Goff, J. A. (2020). Identifying characteristic and anomalous mantle from the complex relationship between abyssal hill roughness and spreading rates. *Geophysical Research Letters*, *47*(11), e2020GL088162. https://doi.org/10.1029/2020gl088162

Goff, J. A., & Jordan, T. H. (1988). Stochastic modeling of seafloor morphology: Inversion of sea beam data for second-order statistics. *Journal of Geophysical Research*, *93*(B11), 13589–13608. https://doi.org/10.1029/jb093ib11p13589

Goldsmith, E. J., & Esler, J. G. (2021). Wave propagation in rotating shallow water in the presence of small-scale topography. *Journal of Fluid Mechanics*, *923*, A24. https://doi.org/10.1017/jfm.2021.573

Gulliver, L., & Radko, T. (2022). Topographic stabilization of ocean rings. *Geophysical Research Letters*, *49*(5), e2021GL097686. https://doi.org/10.1029/2021gl097686

He, J., & Wang, Y. (2024). Multiple states of two-dimensional turbulence above topography. *Journal of Fluid Mechanics*, *994*, R2. https://doi.org/10.1017/jfm.2024.633

Klymak, J. M., Balwada, D., Garabato, A. N., & Abernathey, R. (2021). Parameterizing nonpropagating form drag over rough bathymetry. *Journal of Physical Oceanography*, *51*(5), 1489–1501. https://doi.org/10.1175/jpo-d-20-0112.1

LaCasce, J., Escartin, J., Chassignet, E. P., & Xu, X. (2019). Jet instability over smooth, corrugated, and realistic bathymetry. *Journal of Physical Oceanography*, *49*(2), 585–605. https://doi.org/10.1175/jpo-d-18-0129.1

Lacasce, J. H., Palóczy, A., & Trodahl, M. (2024). Vortices over bathymetry. *Journal of Fluid Mechanics*, *979*, A32. https://doi.org/10.1017/jfm.2023.1084

Marshall, D. P., Williams, R. G., & Lee, M. M. (1999). The relation between eddy-induced transport and isopycnic gradients of potential vorticity. *Journal of Physical Oceanography*, *29*(7), 1571–1578. https://doi.org/10.1175/1520-0485(1999)029<1571:trbeit>2.0.co;2

Mashayek, A. (2023). Large-scale impacts of small-scale ocean topography. *Journal of Fluid Mechanics*, *964*, F1. https://doi.org/10.1017/jfm.2023.305

Mei, C. C., & Vernescu, M. (2010). *Homogenization methods for multiscale mechanics*. World Scientific Publishing.

Metzger, E. J., Smedstad, O. M., Thoppil, P. G., Hurlburt, H. E., Cummings, J. A., Wallcraft, A. J., et al. (2014). US Navy Operational Global Ocean and Arctic Ice Prediction Systems. *Oceanography*, *27*(3), 32–43. https://doi.org/10.5670/oceanog.2014.66

Naveira Garabato, A. C., Nurser, A. G., Scott, R. B., & Goff, J. A. (2013). The impact of small-scale topography on the dynamical balance of the ocean. *Journal of Physical Oceanography*, *43*(3), 647–668. https://doi.org/10.1175/jpo-d-12-056.1

Nikurashin, M., Ferrari, R., Grisouard, N., & Polzin, K. (2014). The impact of finite-amplitude bottom topography on internal wave generation in the Southern Ocean. *Journal of Physical Oceanography*, *44*(11), 2938–2950. https://doi.org/10.1175/jpo-d-13-0201.1

Palóczy, A., & LaCasce, J. H. (2022). Instability of a surface jet over rough topography. *Journal of Physical Oceanography*, *52*(11), 2725–2740. https://doi.org/10.1175/jpo-d-22-0079.1

Parseval, M.-A. (1806). Mémoire sur les séries et sur l'intégration complète d'une équation aux différences partielles linéaires du second ordre, à coefficients constants. *Mémoires présentés par divers savants à l'Académie des Sciences, Paris*, *1*, 638–648.

Pedlosky, J. (1987). *Geophysical fluid dynamics*. Springer.

Pudig, M. P., & Smith, K. S. (2025). Baroclinic turbulence above rough topography: The vortex gas and topographic turbulence regimes. *Journal of Physical Oceanography*, *55*(5), 611–630. https://doi.org/10.1175/jpo-d-24-0110.1

Radko, T. (2020). Control of baroclinic instability by submesoscale topography. *Journal of Fluid Mechanics*, *882*, A14. https://doi.org/10.1017/jfm.2019.826

Radko, T. (2022a). Spin-down of a barotropic vortex by irregular small-scale topography. *Journal of Fluid Mechanics*, *944*, A5. https://doi.org/10.1017/jfm.2022.488

Radko, T. (2022b). Spin-down of a baroclinic vortex by irregular small-scale topography. *Journal of Fluid Mechanics*, *953*, A7. https://doi.org/10.1017/jfm.2022.944

Radko, T. (2023a). A generalized theory of flow forcing by rough topography. *Journal of Fluid Mechanics*, *961*, A24. https://doi.org/10.1017/jfm.2023.169

Radko, T. (2023b). The sandpaper theory of flow-topography interaction for homogeneous shallow-water systems. *Journal of Fluid Mechanics*, *977*, A9. https://doi.org/10.1017/jfm.2023.945

Radko, T. (2024a). The instability of non-monotonic drag laws. *Journal of Fluid Mechanics*, *993*, A13. https://doi.org/10.1017/jfm.2024.635

Radko, T. (2024b). The sandpaper theory of flow-topography interaction for multilayer shallow-water systems. *Journal of Fluid Mechanics*, *988*, A52. https://doi.org/10.1017/jfm.2024.470

Radko, T. (2026). Data for "The Sandpaper Theory of Flow-Topography Interaction: The Non-Local Formulation" [Dataset]. *Figshare*. https://doi.org/10.6084/m9.figshare.30141550

Rhines, P. B., & Young, W. R. (1982). A theory of the wind-driven circulation. Part I: Mid-ocean gyres. *Journal of Marine Research*, *40*(Suppl), 559–596.

Richet, O., Sloyan, B., Nikurashin, M., & Peña-Molino, B. (2025). Why horizontal resolution and bathymetry matter in modeling the Indonesian Seas. *Geophysical Research Letters*, *52*(24), e2025GL118108. https://doi.org/10.1029/2025gl118108

Siegelman, L., & Young, W. R. (2023). Two-dimensional turbulence above topography: Vortices and potential vorticity homogenization. *Proceedings of the National Academy of Sciences*, *120*(44), e2308018120. https://doi.org/10.1073/pnas.2308018120

Stammer, D. (1997). Global characteristics of ocean variability estimated from regional TOPEX/Poseidon altimeter measurements. *Journal of Physical Oceanography*, *27*(8), 1743–1769. https://doi.org/10.1175/1520-0485(1997)027<1743:gcoove>2.0.co;2

Storer, B. A., Buzzicotti, M., Khatri, H., Griffies, S. M., & Aluie, H. (2022). Global energy spectrum of the general oceanic circulation. *Nature Communications*, *13*(1), 5314. https://doi.org/10.1038/s41467-022-33031-3

Vallis, G. K. (2019). *Essentials of atmospheric and oceanic dynamics*. Cambridge University Press.

Vanneste, J. (2000). Enhanced dissipation for quasi-geostrophic motion over small-scale topography. *Journal of Fluid Mechanics*, *407*, 105–122. https://doi.org/10.1017/s0022112099007430

Vanneste, J. (2003). Nonlinear dynamics over rough topography: Homogeneous and stratified quasi-geostrophic theory. *Journal of Fluid Mechanics*, *474*, 299–318. https://doi.org/10.1017/s0022112002002707

Zhang, L. F., & Xie, J. H. (2024). Spectral condensation and bidirectional energy transfer in quasi-geostrophic turbulence above small-scale topography. *Physics of Fluids*, *36*, 8. https://doi.org/10.1063/5.0216337